

Input Site U1381¹

R.N. Harris, A. Sakaguchi, K. Petronotis, A.T. Baxter, R. Berg, A. Burkett, D. Charpentier, J. Choi, P. Diz Ferreiro, M. Hamahashi, Y. Hashimoto, K. Heydolph, L. Jovane, M. Kastner, W. Kurz, S.O. Kutterolf, Y. Li, A. Malinverno, K.M. Martin, C. Millan, D.B. Nascimento, S. Saito, M.I. Sandoval Gutierrez, E.J. Screaton, C.E. Smith-Duque, E.A. Solomon, S.M. Straub, W. Tanikawa, M.E. Torres, H. Uchimura, P. Vannucchi, Y. Yamamoto, Q. Yan, and X. Zhao²

Chapter contents

Background and objectives	1
Operations	2
Lithostratigraphy and petrology	2
Paleontology and biostratigraphy	5
Structural geology	6
Geochemistry	7
Physical properties	9
Paleomagnetism	11
References	13
Figures	14
Tables	51

Background and objectives

The primary objective of Integrated Ocean Drilling Program (IODP) Expedition 344 was to sample and quantify the material comprising the seismogenic zone of an erosive subduction margin. Fundamental to this objective is an understanding of the nature of the sediment and oceanic crust entering the seismogenic zone, the hydrologic system, and the thermal state of the igneous oceanic crust. Site U1381 serves as a reference site on the subducting aseismic Cocos Ridge.

Site U1381 is located on seismic Line BGR99-7 at common midpoint 5740 (Fig. F1) and is ~4.5 km seaward of the deformation front offshore the Osa Peninsula and Caño Island (Fig. F2). This site was chosen for multiple reasons. First, it is located on a local basement high. Basement relief often focuses fluid flow, so data from this site are likely to document the vigor of fluid flow in this area. Second, a clear seismic record of the plate stratigraphy is present at this site. The seismic section shows a 100 m thick sediment section resting on reflective basement interpreted as Cocos Ridge igneous crust. The sedimentary section is composed of pelagic and hemipelagic sediments (Expedition 334 Scientists, 2012). Sediment thickness along the seismic transect (southwest–northeast) is variable and reflects the relief of the Cocos Ridge basement. Third, Site U1381 is far enough from the frontal thrust that it is expected to be reasonably free from the influence of downslope debris flows that might emanate from the convergent margin slope. Finally, Site U1381 is located on the same seismic line as Sites U1412, U1380, and U1379. Paleomagnetic data constrain the age of this portion of Cocos Ridge to 14 Ma (Barckhausen et al., 2001).

During IODP Expedition 334, Site U1381 was cored using the rotary core barrel (RCB) system because the primary objective was recovery of oceanic crust and time constraints precluded advanced piston corer (APC) drilling through the sediment section (Expedition 334 Scientists, 2012). However, a disadvantage of the RCB system is that recovered sediments are highly disturbed. Thus, a primary goal for revisiting this site was to core the sediment section with the APC to obtain more pristine samples. As a result of APC coring, we recovered the uppermost 13 m of sediment that was not recovered during Expedition 334, identified a sediment hiatus of ~9–11 m.y. (see “Paleontology and biostratigraphy”), recovered 84 tephra layers (see “Lithostratigraphy and petrology”), and identified fractures and veins (see “Structural geology”).

¹Harris, R.N., Sakaguchi, A., Petronotis, K., Baxter, A.T., Berg, R., Burkett, A., Charpentier, D., Choi, J., Diz Ferreiro, P., Hamahashi, M., Hashimoto, Y., Heydolph, K., Jovane, L., Kastner, M., Kurz, W., Kutterolf, S.O., Li, Y., Malinverno, A., Martin, K.M., Millan, C., Nascimento, D.B., Saito, S., Sandoval Gutierrez, M.I., Screaton, E.J., Smith-Duque, C.E., Solomon, E.A., Straub, S.M., Tanikawa, W., Torres, M.E., Uchimura, H., Vannucchi, P., Yamamoto, Y., Yan, Q., and Zhao, X., 2013. Input Site U1381. *In* Harris, R.N., Sakaguchi, A., Petronotis, K., and the Expedition 344 Scientists, *Proc. IODP, 344*: College Station, TX (Integrated Ocean Drilling Program). doi:10.2204/iodp.proc.344.103.2013

²Expedition 344 Scientists' addresses.



Operations

Transit to Site U1381

After a 403 nmi transit from Panama, the vessel stabilized over Site U1381 at 0620 h on 26 October 2012. The initial position was at the coordinates of Hole U1381B (8°25.7149'N, 84°9.4805'W; proposed Site CRIS-1A), which was drilled during Expedition 334 in 2011. The vessel was then repositioned 20 m south of those coordinates. The position reference used for dynamic positioning was a combination of GPS signals, as no positioning beacon was deployed at this site. The final location for Hole U1381C was 8°25.7027'N, 84°9.4800'W, in 2064.6 m water depth.

Hole U1381C

There were three main objectives for Hole U1381C. The first objective was to take a continuous sediment record of the sediment overlying the incoming oceanic crust. The second objective was to capture as much of the sediment/basement interface as possible. The final objective was to establish a temperature gradient for the sediment section above oceanic crust. Orientation measurements were taken with the FlexIT tool, and formation temperature measurements were taken with the advanced piston corer temperature (APCT-3) tool. Advancement for Hole U1381C was 103.8 meters below seafloor (mbsf), with 103.5 m cored with the APC system and 0.3 m cored with the extended core barrel (XCB) system (Table T1). Recovery with the APC system was 108.7 m (105%), and recovery with the XCB system was 0.33 m (110%).

Rig floor operations commenced at 0620 h on 26 October 2012. The APC/XCB bottom-hole assembly (BHA) was made up with an APC/XCB C-3 bit. The trip to the seafloor was uneventful. The top drive was picked up, the drill string was spaced out, and the hole was eventually spudded at 2015 h on 26 October. The first attempt at spudding Hole U1381C failed when the APC core barrel contacted something unknown inside the seal bore assembly. After trying twice to pressure up and shear, the core barrel was pulled back to the surface and examined. Damage was noted on the leading edge of the cutting shoe, indicating hard contact with something unknown. An XCB core barrel was picked up and pumped down the hole at 50 strokes per minute. This successfully cleared the BHA of whatever was preventing the APC core barrel from landing properly. The APC core barrel was run back into the hole, and the hole was spudded. APC coring continued until ~0730 h on 27 October, when the basement was reached. The APCT-3 was deployed on Cores 344-U1381C-3H and 5H-7H, and four good temperature curves were recorded. The FlexIT orientation

tool was deployed on Cores 1H-9H with good results. After reaching basement, the APC system was changed to the XCB system and a single short core was cut to confirm and recover basement material. Last core on deck for Hole U1381C was at 0855 h on 27 October. The hole was then terminated, the top drive was set back, and the drill string was tripped from the hole. The seafloor was cleared at 1020 h, and the BHA was secured on the rig floor at 1545 h, ending Hole U1381C and Site U1381 at 1545 h on 27 October. A total of 33.5 h was spent at Site U1381.

Lithostratigraphy and petrology

During Expedition 334, Holes U1381A and U1381B were drilled to investigate the lithostratigraphy and pore water of the overlying sequence on top of the Cocos Ridge basement, as well as the uppermost portions of the adjacent Cocos Ridge. The Cocos Ridge was cored successfully with the RCB; however, the sedimentary section was associated with low recovery (between 42% and 54%). A goal of Expedition 344 was to fully recover the sedimentary succession by coring Hole U1381C to the sediment/basement contact with the APC. Successful coring from 0 to 103.83 mbsf yielded a succession of sediment, sedimentary rocks, and a short interval of basaltic breccia in the lowermost part of the hole. Tephra layer abundance is generally high (84 tephra in total) but is concentrated in the lower part (~40 to ~100 mbsf) of the recovered sedimentary succession. This cored material was divided into five units (Fig. F3; Table T2).

The uppermost part of Hole U1381C is characterized by a predominantly monotonous sequence of hemipelagic silty clay to clay sediment. Unit I (0–55.93 mbsf) comprises a sequence of light greenish gray hemipelagic silty clay containing terrigenous material (lithic fragments, glass shards, and minerals), as well as common to abundant foraminifers and nannofossils. Tephra layers make up ~1.2% of Unit I and are distributed into 18 well-sorted discrete tephra horizons. The boundary between Units I and II at 55.93 mbsf (Section 344-U1381C-7H-1, 33 cm) represents a hiatus of 9–11 m.y. and separates sediments with ages between ~1.9 and ~13.53 Ma (see “[Paleontology and biostratigraphy](#)”).

Unit II (55.93–100.64 mbsf; Sections 344-U1381C-7H-1, 33 cm, to 11H-5, 104 cm) is a 44.71 m thick dark grayish to yellowish brown clayey interval composed of nannofossil-rich calcareous ooze and variable amounts of sponge spicules, foraminifers, and diatoms. Tephra layers (~6% of Unit II) are thickest and most frequent in the uppermost part of the unit. A total of 62 dark brown to gray and sometimes light gray tephra horizons are preserved as discrete layers or individual and/or layered ash pods.

Unit III is a 2.56 m thick interval between 100.64 and 103.20 mbsf (Sections 344-U1381C-11H-5, 104 cm, to 12H-1, 10 cm). This unit is a nannofossil calcareous ooze characterized by an abrupt decrease in the abundance of sponge spicules and foraminifers and an increase in clay content. Reworked clay clasts from the underlying Unit IV can be found in the lowermost 10 cm. Tephra layers and pods are rare (<1%) in this interval, and only four dark brown layers were recovered.

Unit IV is a 0.35 m thick interval between 103.20 and 103.55 mbsf (Sections 344-U1381C-12H-1, 10 cm, to 12H-CC, 16 cm) and consists of a dark brown sequence of well-consolidated clay and lithified claystone almost completely devoid of biogenic components. Unit V, cored to a total depth of 103.83 mbsf (Section 344-U1381C-13X-1, 0–33 cm), is a 33 cm thick basalt breccia.

Description of units

The cores recovered from Hole U1381C are divided into five lithostratigraphic units (Fig. F3; Table T2) that span the 103.55 m cover sequence above the basement, as well as the interface with the basaltic breccia below.

Unit I

Interval: Sections 344-U1381C-1H-1, 0 cm, to 7H-1, 33 cm

Thickness: 55.93 m

Depth: 0–55.93 mbsf

Age: early Pleistocene to recent

Lithology: soft silty clay to clay sediment

Unit I consists mainly of massive, light greenish gray, soft (silty) clay sediment with minor changes in the proportions of clay and silt in the background sedimentation (Fig. F4). Biogenic components, especially nannofossils and diatoms, are abundant throughout the unit. Silt-sized grains in smear slides include common clastic components such as plagioclase, chert, chlorite, pyroxene, amphibole, opaque minerals, calcite, glauconite, glass, and rare quartz, as well as traces of biogenic fragments such as radiolarians, foraminifers, and sponge spicules. Eighteen well-sorted tephra layers ranging in thickness from 1 to 7 cm are normally graded and moderately disturbed and smeared out by drilling operations (Figs. F5, F6).

Unit II

Interval: Sections 344-U1381C-7H-1, 33 cm, to 11H-5, 104 cm

Thickness: 44.71 m

Depth: 55.93–100.64 mbsf

Age: early Miocene

Lithology: nannofossil calcareous ooze with sponge spicules

Unit II mainly consists of dark grayish to yellowish brown, soft to hardened silty clayey calcareous ooze with abundant sponge spicules and varying amounts of foraminifers (Fig. F7). Unit II is distinguished from Unit I by its abundant biogenic content, which is also reflected in the abrupt change in color. The sediment contains >70% organic components such as spicules, diatoms, radiolarians, and nannofossils, with the abundance of clay and calcareous components increasing with depth. Mineral components that occur in trace amounts include feldspar, pyroxene, olivine, calcite, and opaque minerals. Sixty-two tephra horizons, ranging from 1 to 41 cm in thickness, are massive and soft, show normal gradation from medium sand to silt, and occur as discrete layers, individual ash pods, or ash pod layers (Figs. F8, F9). These horizons are well sorted, which is typical of marine tephra (e.g., Carey, 1997), and some are partially disturbed and smeared by bioturbation and drilling at their base. In general, the abundance and thickness of these predominantly mafic tephra layers decreases with depth.

Unit III

Interval: Sections 344-U1381C-11H-5, 104 cm, to 12H-1, 10 cm

Thickness: 2.56 m

Depth: 100.64–103.20 mbsf

Age: middle Miocene

Lithology: nannofossil ooze

The boundary between Units II and III displays a clear change from dark grayish to yellowish brown sediment to a dark brown color and finer grained nannofossil-dominated clay (Fig. F10). Minor matrix components include rare glass shards and feldspar crystals. The lowermost part of this unit (interval 344-U1381C-12H-1, 0–10 cm) contains laminations ~5 mm in scale, as well as abundant well-rounded dark greenish black claystone clasts that are most likely reworked material from Unit IV, below (Fig. F11). Four tephra layers were identified in this unit.

Unit IV

Interval: Sections 344-U1381C-12H-1, 10 cm, to 12H-CC, 16 cm

Thickness: 0.35 m

Depth: 103.20–103.55 mbsf

Age: middle Miocene

Lithology: claystone

Unit IV consists of a dark greenish black, 35 cm thick sequence of very consolidated and partly lithified clay to claystone (Fig. F11). This unit contains only

trace amounts of nannofossils and lacks any other biogenic components. The entire sedimentary sequence is highly disturbed and fractured by drilling.

Unit V

Interval: Section 344-U1381C-13X-1, 0–33 cm

Thickness: 0.33 m

Depth: 103.50–103.83 mbsf

Age: middle Miocene

Lithology: basaltic breccia

Unit V consists of rubble with preserved matrix in the uppermost 5 cm, followed by poorly sorted brecciated basaltic fragments varying from 1 mm to 10 cm in size (Fig. F12). No obvious contact between Units IV and V was recovered.

Basaltic clasts and rubble throughout Unit V range from sparsely to highly plagioclase-clinopyroxene phyric, whereas textures may vary from variolitic to intersertal. Groundmass composition consists of microcrystalline plagioclase and pyroxene with accessory Fe-Ti oxides. Many fragments exhibit curved chilled margins with fresh to devitrified glassy rims. Approximately 10% of the groundmass is made up of euhedral- to anhedral-shaped plagioclase phenocrysts that range in size from 0.1 to 4 mm. Vesicles represent 3% of the recovered basaltic fragments and are typically irregular but well rounded. Vesicle abundance in larger clasts and rubble is greatest near the chilled margins.

Overall alteration of the basaltic groundmass is slight to moderate, with smectite replacing interstitial glass and partially corroding plagioclase and clinopyroxene phenocrysts. Black halos near the chilled margins and flanking veins are composed of secondary pyrite. Within the main rubble interval (344-U1381C-13X-1, 15–33 cm), larger fragments preserve narrow (<0.1 mm) veins of sulfides and smectite, whereas smaller fragments may be partially to completely covered by sulfides. Vesicles within the basaltic rubble are 50% filled by smectite and are typically flanked by narrow pyrite halos. The vein and vesicle mineralization sequence implied from thin section analyses suggests that sulfide mineralization predates smectite.

Matrix mineralogy observed from smear slides in the uppermost part of the unit (interval 344-U1381C-13X-1, 0–5 cm) includes undefined clay minerals, plagioclase, clinopyroxene, and pyrite, implying that the matrix is basaltic in origin, tentatively the result of extensive alteration of a lava flow collapse.

Tephra layers

A total of 84 tephra layers are recognized in Hole U1381C. These tephra layers are intercalated with

sediment from background Unit I (18 tephras), Unit II (62 tephras), and Unit III (4 tephras). Individual tephra layers range in thickness from 1 to 41 cm. Unconformable and/or inclined bedding is rare. Most of the tephra layers are well sorted and have a sharp basal contact with the underlying sediment but a gradual transition with the overlying, ash-bearing sediment. Normal grading can often be seen in the tephra horizons and even in the large ash pods. Some tephra layers are lithified (Figs. F8, F9). In some cores, localized bioturbation is observed at the tephra layer boundaries (Fig. F6). Drilling disturbance rarely overprints the original structure of the tephra layers (Fig. F9). Aside from the greater abundance of tephra horizons in the upper part of Unit II, no systematic features were correlated with depth.

The compositions of the 84 identified tephra layers seem to be variable, as evident from the gray to pinkish (more felsic, silica rich; predominantly Unit I; e.g., Figs. F5, F6) and brownish black (more mafic, silica-poor; predominantly Unit II; e.g., Figs. F8, F9) colors. Dark black mafic tephra beds account for ~27% of the total tephra bed assemblage of Unit I in Hole U1381C but are more abundant in Unit II (~72%). Unit I tephras have mineral assemblages similar to those observed during Expedition 334 in Holes U1378B, U1379C, and U1380A.

Light-colored felsic tephra layers contain mainly transparent glass shards that are mostly fresh with few signs of alteration, as well as pumiceous clasts. Devitrification structures within glass shards increase with depth, reflecting increasing alteration with depth. Grain size ranges from very fine to coarse ash (up to millimeter sized). The mineral assemblages consist of plagioclase, pyroxene, hornblende, and biotite. Plagioclase is the dominant phenocryst phase, but some tephras are dominated by amphibole and biotite.

Dark gray mafic tephra layers consist predominantly of very coarse (up to 3 mm), dark to light brown sideromelane glass shards and rare tachylitic particles. Most of the glass shards have blocky shapes and are medium to poorly vesicular but also show tubular-like glass shards. The mineral assemblages of the black mafic tephras in Unit II include rare plagioclase and traces of pyroxene and olivine, but in general, the number of phenocrysts is much lower than in tephras found in Unit I. Glass shards are increasingly affected by alteration in the deeper part of the hole.

X-ray diffraction analysis

Preliminary X-ray diffraction analysis of sediment samples from Hole U1381C (Fig. F13) suggests there is little variation in composition within each lithostratigraphic unit (Fig. F14).

X-ray diffractograms of Unit I indicate that the major mineral components are phyllosilicates, including chlorite and smectite, calcite, Ca- and Na-plagioclase, and quartz (Fig. F13). The relative abundances of major minerals in Unit I are constant overall, with a slight decrease of quartz and associated increase of calcite toward the base (Fig. F14). Amphibole (hornblende), pyroxene (diopside), zeolites (stilbite and laumontite), and pyrite peaks are also present. Biotite is present in some samples in the lower part of the unit (Cores 344-U1381C-4H and 6H), sometimes in large amounts.

Variation in mineral composition is most strongly noted in the sandy sediment collected from Unit I and the upper section of Unit II, where biogenic fragments are more common (Fig. F14). Samples from Unit II produced spectra dominated by calcite and Mg-rich calcite with pyrite. Common Ca- and Na-plagioclase and rare quartz are also present throughout Unit II (Fig. F13).

X-ray diffractograms of samples from Unit III (Figs. F13, F14) indicate that the major mineral components are calcite, zeolite (Ca-heulandite), and smectite. Plagioclase and pyrite are present as minor phases. The vein sample in Section 344-U1381C-11H-7 is composed of zeolite and smectite.

Unit IV comprises a mixture of smectite (most likely saponite), pyrite, and minor plagioclase (Fig. F14). Sphalerite, calcite, and anhydrite are present as minor occasional phases.

Depositional environment and correlation to Hole U1381A

The cover sequence recovered from Hole U1381C consists of a sequence of hemipelagic silty clay with terrigenous input, presumably remobilized from the slope sediment sequence, overlying sponge spicule-rich nannofossil calcareous ooze, pelagic calcareous ooze, and pelagic claystone. The lithologic occurrence and the depth ranges of the unit boundaries are similar to Hole U1381A, drilled during Expedition 334. The conspicuous, large hiatus between hemipelagic Unit I and pelagic Unit II (see “Paleontology and biostratigraphy”) was also found at Site 1242 (Ocean Drilling Program [ODP] Leg 202) but differs in boundary ages (Pliocene to middle Miocene) and the absence of the characteristic mafic tephra layers found in Unit II.

Paleontology and biostratigraphy

Calcareous nannofossil and radiolarian assemblages observed at Site U1381 provide biostratigraphic in-

formation for the cored sediment. Benthic foraminifer assemblages are used to characterize paleoenvironmental changes throughout the depositional history of the cored sediment.

Calcareous nannofossils

Two main sequences have been identified based on nannofossil biostratigraphy. The first is a Pleistocene to recent sequence that corresponds to Unit I. The second is a Miocene sequence that corresponds to Unit II. The hiatus between Units I and II is tentatively estimated to be ~11 m.y.

Nannofossils were observed in all core catcher samples from Cores 344-U1381C-1H through 12H. Overall preservation is good to moderate. The interval from 0 to 18.11 mbsf is assigned to nannofossil Zone NN21, based on the presence of *Emiliana huxleyi* in Sample 344-U1381C-2H-CC. *Calcidiscus leptoporus*, *Gephyrocapsa oceanica*, *Gephyrocapsa caribbeanica*, and *Helicosphera carteri* are species indicative of this assemblage. The presence of the planktonic foraminifer *Globigerinoides ruber* (pink) in this sample indicates that this section is older than 120 ka (last occurrence [LO] of *G. ruber* [pink]) and younger than 290 ka (first occurrence of *E. huxleyi*). A single *Discoaster* sp. specimen identified in this sample suggests reworking of older material. The interval from 18.11 to 46.62 mbsf is constrained to Zones NN19–NN21, based on the presence of *C. leptoporus*, *G. oceanica*, *G. caribbeanica*, and *H. carteri* and the absence of *E. huxleyi*.

The interval from 46.62 to 56.13 mbsf is tentatively assigned to nannofossil Zone NN19, based on the occurrence of *Pseudoemiliana lacunosa* in Sample 344-U1381C-6H-CC. Further biostratigraphic data for this sample are provided by benthic foraminifers. The extinction of the *Stilostomella* group has been assigned to the late early and middle Pleistocene (~1.2–0.6 Ma; Hayward, 2002). Sample 344-U1381C-6H-CC contains the LO of representatives of this group (Table T3), suggesting that the minimum age of the sediment is >0.6 Ma and the maximum age of the sediment, just above the lithologic boundary between Units I and II, is 1.89 Ma. However, according to the sediment accumulation rate estimated for Unit I (80–100 m/m.y.), the lower interval may be closer to 1 Ma.

A major change in nannofossil assemblage occurs between Samples 344-U1381C-6H-CC and 7H-CC, represented by the disappearance of the genus *Gephyrocapsa* and the appearance of *Sphenolithus*. Samples 344-U1381C-7H-CC through 12H-CC are assigned to Zone NN5 (13.53–14.91 Ma), based on the presence of *Sphenolithus heteromorphus*, *Sphenolithus*

moriformis, *Coccolithus miopelagicus*, *Discoaster exilis*, and *Discoaster deflandrei*.

In order to better estimate the hiatus between Units I and II, 10 samples were taken across the lithologic boundary. Preliminary results indicate that a 60 cm zone of reworked material with a mixed assemblage is present across the unit boundary, consistent with a zone of bioturbation (see “[Lithostratigraphy and petrology](#)”). The lowermost sediments of Unit I contain similar assemblages to those found in Sample 344-U1381C-6H-CC and are indicative of Zone NN19. However, a number of genera, such as *Discoaster* spp. and some radiolarians (*Didymocyrtis antepenultima* and *Didymocyrtis laticonus*), are also found in these samples and indicate reworking of older sediments. The uppermost portion of Unit II is also heavily bioturbated, but the undisturbed (Zone NN5) pelagic sedimentation resumes 30 cm below the boundary. A hiatus of ~11 m.y. is recorded between Units I and II.

Radiolarians

Radiolarians were present in all recovered cores with the exception of Samples 344-U1381C-11H-CC and 12H-CC. Overall, the siliceous fraction was dominated by radiolarians and diatoms, with a minor proportion of sponge spicules. Radiolarians were generally well preserved.

Observations of radiolarians indicate two distinct assemblages in Hole U1381C (Fig. [F15](#); Table [T4](#)). The upper assemblage (Samples 344-U1381C-1H-CC through 6H-CC) represents a Pleistocene–Holocene sequence that corresponds to Unit I. Detailed biostratigraphic zonations could not be assigned to this assemblage because of the lack of biostratigraphically important species. However, the presence of *Amphirhopalum ypsilon* in Samples 344-U1381C-1H-CC through 4H-CC suggests a depositional age <1 Ma (Zone RN14; Sanfilippo and Nigrini, 1998).

The lower assemblage (Samples 344-U1381C-7H-CC through 10H-CC) is representative of the early to middle Miocene and corresponds to Unit II. The presence of *D. antepenultima* and *D. laticonus* in Samples 344-U1381C-7H-CC and 8H-CC is indicative of the early late Miocene (Zones RN6 and RN5). Samples 344-U1381C-9H-CC and 10H-CC are constrained to the late early Miocene (Zone RN5) because of the presence of *Didymocyrtis violina* (Sanfilippo and Nigrini, 1998). Radiolarian biostratigraphy suggests a hiatus of ~9 to 11 m.y. between Units I and II, consistent with the hiatus seen in nannofossil biostratigraphy. Using the estimates from nannofossil and radiolarian biostratigraphy, a range of 9–11 m.y. is proposed for the duration of the hiatus.

Benthic foraminifers

Benthic foraminifers (B) were studied in core catcher samples from Cores 344-U1381C-1H through 11H (Table [T5](#)). All samples, with the exception of Sample 344-U1381C-11H-CC, which is well indurated, consist of loose sediment dominated by planktonic foraminifers (P) ($P/[P + B] > 0.8$). Benthic foraminifer assemblages indicate that two different environments are represented in Hole U1381C, as also indicated by biostratigraphic and lithostratigraphic data (Fig. [F16](#)).

The upper interval (Samples 344-U1381C-1H-CC through 6H-CC) corresponds to Unit I and is dominated by species of the genera *Uvigerina* (*Uvigerina peregrina*, *Uvigerina auberiana*, and *Uvigerina* cf. *senticosa*) and *Siphouvigerina* (*Siphouvigerina ampullacea*), with minor relative abundances of *Chilostomella oolina*, *Cibicidoides pachyderma*, and *Fontbotia wuellerstorfi*. This assemblage is characteristic of bathyal environments with a moderate to high flux of organic carbon to the seafloor (Goody and Rathburn, 1999).

The lower interval (Samples 344-U1381C-7H-CC through 11H-CC) contains a substantially different assemblage than Unit I. Characteristic species found in this interval include *C. oolina*, *F. wuellerstorfi*, *Uvigerina* sp., *Gyroidinoides* sp., and *Globocassidulina subglobosa*, together with a diverse group of elongated foraminifers belonging to genera such as *Stilostomella*, *Plectofrondicularia*, *Pleurostomella*, *Siphonodosaria*, and *Crysalogonium*. The presence of species that occupy a wide microhabitat range (*F. wuellerstorfi*, *C. pachyderma*, and *C. oolina*) might suggest a bathyal environment with low to moderate flux of organic carbon and suboxic to anoxic conditions present at the time the deeper sediment layers were deposited (Goody and Rathburn, 1999; Corliss, 1985).

Structural geology

The primary structural geology goal during Expedition 344 was to describe and document the style, geometry, and kinematics of structural features observed in the cores. Hole U1381C consists of cores from the sedimentary sequence (~105 m) and ends at the boundary to the underlying oceanic basement basalt of the Cocos plate (Table [T2](#)).

Bedding was determined throughout the sedimentary sequence. The bedding dips vary from subhorizontal to gentle with a maximum value of 30° (Fig. [F17](#)). Sediment near the contact with the Cocos plate oceanic basement shows deformation bands, zeolite- and/or smectite-filled extensional fractures, and shear fractures.

Structures within the sedimentary sequence

Bedding dips were observed and measured in the sediment cores retrieved from Hole U1381C (Figs. F17, F18). Dip angles are generally subhorizontal in Unit I. In Unit II, a few dip angles vary between 20° and 31°. Bedding plane orientations were determined mostly on tephra layers, some of which show sharp scoured bases (Fig. F19). Erosional processes linked to the submarine flow of tephra are assumed to result in steeper than usual dip angles of bedding planes. Attitudes of bedding planes were restored to geographic coordinates using paleomagnetic data (Fig. F18). Restored bedding orientation data still show subhorizontal orientation without preferred attitude in Unit I. Unit II bedding planes preferentially dip gently either east or west.

Distinct brittle deformation was observed in Unit III. Subhorizontal to steeply dipping deformation bands were observed in interval 344-U1381C-11H-5, 103–118 cm (Fig. F20). The deformation bands trend roughly ENE–WSW, subparallel to the trend of the Cocos Ridge (Fig. F21). Mineral-filled extensional fractures and shear fractures were observed in Sections 344-U1381C-11H-6 and 11H-7 (Fig. F20). Both types of fractures dip steeply (vertical to subvertical) and strike NNE–SSW. The shear fractures show a normal component of shear (Fig. F21). Displacement is at the scale of millimeters to >10 cm.

Geochemistry

For pore fluid geochemistry measurements, we collected 20 whole-round samples that were 10 cm long and 8 that were 15 cm long, at a frequency of 2–4 samples per core. These samples were stored and cleaned in a N₂ glove bag to remove drilling contamination. The cleaned samples were placed in Ti squeezers and squeezed at gauge forces up to 30,000 lb. The inner diameter of the Ti squeezers is 9 cm; thus, the maximum squeezing pressure was 3043 psi (~21 MPa). The pore fluid was collected in syringes and filtered prior to analysis. The volume of pore fluid recovered varied with lithology and burial depth from 22 mL to a maximum of 72 mL in lithostratigraphic Unit II (see “[Lithostratigraphy and petrology](#)”). Specific aliquots were used for shipboard analyses, and the remaining fluid was sampled for shore-based analyses, following protocols specified by the scientists that will be involved in these analyses (see the “[Methods](#)” chapter [Harris et al., 2013]). Three additional 10 cm long whole rounds were acquired from Sections 344-U1381C-7H-6, 9H-6, and 11H-1 for He isotope analyses. These samples were handled on the lower tween deck to avoid con-

tamination with gas tank He present in the Chemistry Laboratory. They were stored and cleaned in a N₂ glove bag at 4°C, squeezed as described above, and stored in Cu tubes that were crimped tightly.

For gas analyses, 29 headspace samples were collected using a 5 mL cut-off syringe directly adjacent to the pore water sample. Samples were analyzed following the protocol described in “[Geochemistry](#)” in the “[Methods](#)” chapter (Harris et al., 2013).

In addition, 28 sediment samples were collected from the working half of the core, adjacent to the pore water samples. These samples were freeze-dried, ground, and analyzed for inorganic carbon (IC), total carbon (TC), and total nitrogen (TN) concentrations.

Inorganic geochemistry

Salinity, chloride, and alkalis (sodium and potassium)

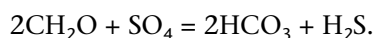
Downhole profiles of salinity, chloride, sodium, and potassium in Hole U1381C are shown in Figure F22, which includes data collected from Hole U1381B during Expedition 334 for comparison (Expedition 334 Scientists, 2012) (Table T6). From the seafloor to ~22 mbsf, salinity has a seawater value of 35.0 and shows slightly lower values (34.0–34.5) to ~100 mbsf. The lowest salinity value of 33.5 was obtained in the lowermost ~15 m of this site, above the sediment/basement contact where the sediment is more indurated. Chloride concentrations are slightly below the modern seawater value (559 mM) in the uppermost ~7 m (554–557 mM), are equal to modern seawater at ~14 mbsf, and are 1%–2% (561–570 mM) higher than modern seawater between ~15 and 95 mbsf. This slight increase in chloride concentration is most likely caused by minor hydration reactions of volcanic tephra to clay minerals. Similar to salinity, Cl concentrations slightly decrease above the sediment/basement contact.

Sodium concentrations range between 462 and 479 mM throughout the cored section (Fig. F22). Only three samples have near-seawater Na concentrations (480 mM). It is interesting to note that at this site, Na behaves differently from Cl, possibly because of volcanic tephra alteration reactions. Potassium concentrations decrease from a seafloor value of 12.2 mM (17% higher than the modern seawater value of 10.4 mM) to the sediment/basement interface, where they reach modern seawater concentrations (Fig. F22). Higher concentrations of K than in modern seawater have been observed at numerous sites near the seafloor and have been attributed to ion exchange with clay minerals where ammonium values are elevated and to volcanic ash alteration. The latter reaction, however, could also be responsible

for decreasing K concentrations at greater depths (see “[Lithostratigraphy and petrology](#)”).

Alkalinity, sulfate, ammonium, calcium, and magnesium

The alkalinity and sulfate depth profiles are approximate mirror images of each other (Fig. F23) and are caused by oxidation of organic matter according to the simplified reaction



Alkalinity reaches a maximum value of 17.4 mM at ~32 mbsf, and the sulfate minimum value of 12.1 mM was observed at 36–41 mbsf. Elevated alkalinities cause carbonate precipitation, as indicated by a decrease in Ca (and Mg) concentrations at the same depth interval, as discussed below. Organic matter diagenesis in the uppermost part of the sediment section is also observed in the ammonium concentration-depth profile, which mimics the alkalinity profile. Ammonium reaches a maximum value of 1.6 mM at the depth of the alkalinity maximum (32 mbsf) and decreases nearly linearly to 0.29 mM at the base of the hole (Fig. F22). Below this maximum value at ~32 mbsf, alkalinity concentrations also decrease to a minimum of ~2.7 mM near the sediment/basement interface. In contrast, sulfate concentrations increase to 25 mM in the deepest sample, which is close to the modern seawater value of 28.9 mM. The observation of an increase in dissolved sulfate at depth indicates that the diffusion of sulfate from basement into the sediment section is faster than the rate of microbial sulfate reduction. A similar sulfate concentration-depth profile was observed at the reference sediment section offshore Nicoya Peninsula, at ODP Leg 170 Site 1039 (Kimura, Silver, Blum, et al., 1997) and in Expedition 334 Hole U1381B (Expedition 334 Scientists, 2012). The increase in sulfate concentrations in the deeper section is evidence for diffusional communication of the sediment column with fluid in the oceanic basement.

Both Ca and Mg concentrations are slightly depleted at ~1.5 mbsf, the shallowest pore fluid sample obtained, and continue to decrease parallel to the increasing alkalinity pattern (Fig. F23), suggesting carbonate diagenesis. In the shallowest pore fluid sample, the Ca concentration is 9.6 mM instead of the modern seawater value of 10.55 mM and the Mg concentration is 49.5 mM instead of the modern seawater value of 54 mM. The depletion in Mg is more than four times that of Ca, suggesting that more than one diagenetic reaction controls Mg (i.e., carbonate diagenesis, clay ion exchange, and minor ash alteration). Ca continues to decrease downhole to

the depth of maximum alkalinity and minimum sulfate concentrations, suggesting further precipitation of authigenic carbonates in the zone of active sulfate reduction and alkalinity production. The Mg profile, however, remains almost constant in this depth range (Fig. F23). The consumption of Mg by carbonate diagenesis may be countered by an Mg increase due to ion exchange in clay minerals driven by the produced ammonium. Below this calcium consumption depth, Ca concentrations increase downhole to a maximum of 16.2 mM at the sediment/basement interface (~150% modern seawater value). The increase in Ca with depth likely reflects both ash alteration in the sediment column and diffusional interaction with an altered basement fluid. Because basement fluids are depleted in Mg, diffusional interaction with the basement fluid should decrease the Mg concentration with depth; however, Mg concentrations remain almost constant to the bottom of the hole. A combination of reactions involving volcanic tephra alteration and clay ion exchange may explain the observed unusual Mg concentration profile. Reaction modeling will be required to explain the controlling reactions of Mg in this hole.

Concentrations of phosphate, an important nutrient (the Redfield ratio of marine organic matter is ~106C:16N:1P), increase rapidly from a seafloor value of ~2 μM to a maximum of ~38 μM, which corresponds in depth to the maximum in alkalinity concentration. Below this depth, phosphate decreases sharply, and in sediments corresponding to lithostratigraphic Unit II (see “[Lithostratigraphy and petrology](#)”), pore fluid phosphate concentrations are very low, just 1–2 μM.

Strontium, lithium, magnesium, silica, boron, and barium

Downhole distributions of Sr, Li, Mn, Si, B, and Ba are shown in Figure F24, which includes data collected from Hole U1381B during Expedition 334 (M.E. Torres et al., unpubl. data) for comparison (Table T7). Sr concentrations are close to a modern seawater value of 87 μM from the seafloor to ~45 mbsf and increase slightly downhole from ~45 to ~95 mbsf to a maximum concentration of 108 μM. In the deepest ~10 m of the hole, however, Sr concentrations decrease slightly, reaching ~104 μM at the sediment/basalt interface. The minor decrease in Sr concentrations observed at the base of the hole must be related to reactions in the oceanic basement. Shore-based Sr isotope data will identify the source(s) of Sr below ~45 mbsf.

Li is highly sensitive to volcanic tephra alteration and to the temperature of the alteration reaction. In the uppermost ~25 m, Li concentrations decrease

from 25 μM (approximately the seawater value of 26 μM) to a minimum of 21 μM at 17 mbsf (Fig. F24), probably because of low-temperature minor tephra alteration. Deeper in the sediment, Li concentrations increase to a maximum of ~ 40 μM at the bottom of the hole. This concentration-depth profile suggests diffusional interaction with fluid at a greater depth, where higher temperatures prevail. Concentrations of Li, one of the most “fluid-loving” elements, increase with increasing temperatures during silicate-fluid diagenetic reactions.

Concentrations of Mn, a redox-sensitive element, decrease in the uppermost ~ 25 m, the zone of active sulfate reduction (Fig. F24). Usually in this zone, Mn concentrations increase with increasing sulfate reduction; oxidized Mn is being reduced and released into the pore fluid as Mn^{2+} , a more soluble species than oxidized Mn. The decrease in Mn concentrations thus suggests diagenetic uptake of Mn; it most likely co-precipitates with the diagenetic carbonates. From ~ 25 mbsf to the bottom of the hole, Mn concentrations increase with depth, similar to the Li profile. This Mn increase has a diffusional shape, suggesting communication with deeper fluid in the oceanic basement that has a higher Mn concentration.

In the shallowest sample analyzed at ~ 1.5 mbsf, Si concentrations (523 μM) are higher than bottom water concentration, which in this region is ~ 225 μM Si. Silica concentrations increase with depth to ~ 1000 μM (Fig. F24). Dissolution of siliceous phyto- and zooplankton diatoms, radiolarians, and sponge spicules observed in larger abundances in lithostratigraphic Unit II (see “[Lithostratigraphy and petrology](#)”) is responsible for the high Si concentrations. The solubility of nonbiogenic silicates, such as feldspars, is only ~ 400 – 500 μM at $\sim 25^\circ\text{C}$, the estimated temperature at the bottom of the hole. Si solubility increases with increasing temperature.

Ba concentrations throughout the sediment section are very low, between ~ 200 and 530 μM , slightly above the bottom seawater concentration of ~ 200 – 300 μM . These concentrations are typical of pore fluid Ba values in the pelagic environment, where sulfate concentrations are too high for barite remobilization. No obvious trends are observed in the Ba concentration-depth profile, as expected for this environment.

In summary, the concentration-depth profiles of Ca and SO_4 , as well as those of Li and Mn and possibly Si, indicate diffusional interaction with altered seawater fluid in the oceanic basement. The Sr profile, however, shows a reversal close to the sediment/basement contact, suggesting that fluid-basement reactions are influencing the reversal in the Sr profile.

Organic geochemistry

Organic geochemistry data for Hole U1381C are listed in Table T8 and plotted in Figures F25 and F26. In the headspace gases, methane concentrations range from 2 to 262 ppmv. Ethane concentrations range between 2 and 256 ppmv. We observed the highest methane concentrations in the shallowest sample at 1.5 mbsf, together with high levels of ethane and propane. This observation likely indicates potential contamination of the sediment sample by drilling fluid or during sampling on the catwalk. In all other samples, methane concentration was < 7 ppmv, and no heavy hydrocarbons were detected.

The IC distribution (Table T9), shown in Figure F26, shows increasing concentrations from < 2 to ~ 6 wt% at 55 mbsf, consistent with observed changes from the silty clay sediment of lithostratigraphic Unit I to the foraminiferal carbonate ooze of lithostratigraphic Unit II (see “[Lithostratigraphy and petrology](#)”). TC concentrations also increase from ~ 3 to < 7 wt% at that depth. Total organic carbon concentrations range from 0.97 to 2.1 wt%. TN concentrations range between 0.049 and 1.7 wt%. TN concentrations are highest between 30 and 44 mbsf.

Physical properties

At Site U1381, physical properties measurements were made to help characterize lithostratigraphic units. After sediment cores reached thermal equilibrium with ambient temperature at $\sim 20^\circ\text{C}$, gamma ray attenuation (GRA) density, magnetic susceptibility, and P -wave velocity were measured using the Whole-Round Multisensor Logger (WRMSL). After WRMSL scanning, the whole-round sections were logged for natural gamma radiation (NGR) and thermal conductivity was measured using the full-space method on sediment cores. After splitting the cores, a digital imaging logger and a color spectrophotometer were used to collect images of the split surfaces and magnetic susceptibility was measured on the archive-half cores. Moisture and density (MAD) were measured on discrete samples collected from the working halves of the split sediment cores, generally once per section. Electrical conductivity, P -wave velocity, and shear strength were measured on the working halves of split cores, generally once per section. Discrete physical properties measurements were taken near the base of the section to be adjacent to whole-round cores taken for interstitial water or postcruise geotechnical studies. Measurements on Unit V (basement) do not include magnetic susceptibility, NGR, MAD, electrical conductivity, P -wave velocity, and shear strength because of core disturbance.

Density and porosity

Bulk density values in Hole U1381C were determined from both GRA measurements on whole cores and mass/volume measurements on discrete samples from the working halves of split cores (see “**Physical properties**” in the “Methods” chapter [Harris et al., 2013]). In general, wet bulk density values determined from whole-round GRA measurements and measurements from discrete samples agree well, with whole-round GRA measurements showing greater scatter (Fig. F27A). Grain density measurements were determined from mass/volume measurements on dry discrete samples within the sedimentary sequence. Grain density values average 2.7 and 2.5 g/cm³ within lithostratigraphic Units I and II, respectively (Fig. F27B). Porosity was determined from mass/volume measurements on discrete samples using MAD Method C on sediment cores (see “**Physical properties**” in the “Methods” chapter [Harris et al., 2013]). Porosity values slightly decrease with depth within Unit I, exhibiting very little compaction, and then increase at the Unit I/II boundary (Fig. F27C). In general, porosity values are high, averaging 75% and 78% in Units I and II, respectively. Because porosity is determined based on water mass removed during oven drying, reported porosity values are not true interstitial porosity but include water held in minerals that was removed at 105°C. MAD results from Hole U1381C show similar trends to those from Holes U1381A and U1381B but show less scatter and are more complete because of the better core recovery and reduced core disturbance of APC coring.

Magnetic susceptibility

Volumetric magnetic susceptibilities were measured using the WRMSL, and point measurements were made on the Section Half Multisensor Logger (SHMSL) for all recovered sediments (Units I–IV) from Hole U1381C. No magnetic susceptibility track data were acquired in the basement (Unit V). Similar trends were observed in magnetic susceptibility values measured with these two instruments (Fig. F28). Hole U1381C magnetic susceptibility data are continuous from the seafloor to the basement contact, allowing greater interpretation of sediments than Expedition 334 data (Holes U1381A and U1381B; Expedition 334 Scientists, 2012). In the uppermost 10 m, magnetic susceptibility values rapidly increase and then decrease from >170 instrument units (IU) to near 25 IU. Below 10 mbsf, baseline values range between 15 and 25 IU with intermittent peaks of >100 IU. These peaks are interpreted as ash layers and become more frequent with depth down to the Unit I/II boundary. Unit II is characterized by magnetic susceptibility values near zero with a few spikes. These spikes,

which are interpreted as ash layers, are thinner than those observed in Unit I. Also in Unit II, point measurements are generally higher than volumetric measurements but record fewer of the spikes. A spike to >1000 IU in the WRMSL data at the top of Core 344-U1381C-11H (93.6 mbsf) was caused by a sheared metal pin that was later discovered in the core, and this data point is not shown on Figure F28. SHMSL point measurements do not record this spike because this section was rerun after the removal of the pin. Lithostratigraphic Units III and IV have low magnetic susceptibility (averaging 9 IU), with no spikes.

Natural gamma radiation

NGR counting periods were 10 min, and measurement spacing was fixed at 20 cm in all core sections. NGR results are reported in counts per second (cps) (Fig. F29). NGR measurements were not made in the basal sediment and basement (Cores 334-U1381C-12H and 13H) because of core disturbance. NGR counts gradually increase with depth from 10 to 40 mbsf and are highly variable between 40 and 60 mbsf (near the Unit I/II boundary). Below ~60 mbsf (most of Unit II and all of Units III and IV), NGR counts are lower than those within Unit I. The lowest counts, around 10 cps, were observed near the Unit II/III boundary and increase within Unit III.

P-wave velocity

P-wave velocity in Hole U1381C was measured on sediment whole rounds using the WRMSL and on the working halves of sediment split cores using the P-wave velocity gantry (Fig. F30). Discrete measurements of P-wave velocity average 1520 m/s in Unit I (silty clay). In Unit II, P-wave velocities are slightly higher, averaging 1540 m/s, despite the higher measured porosity (Fig. F27C). P-wave velocity increases to 1620 m/s in Unit III (calcareous clay) and decreases to 1560 m/s in Unit IV (claystone). P-wave velocity measured by the WRMSL shows a similar trend to that measured on working halves, although WRMSL P-wave velocity is slightly slower (Fig. F30B). P-wave velocity values on the y - and z -axes were measured only in the shallower interval because of poor waveforms due to brittle cracking in the deeper interval. No significant anisotropy was observed in the measured interval (Fig. F30A).

Thermal conductivity

Thermal conductivity measurements were conducted on sediment whole-round cores using the needle-probe method (see “**Physical properties**” in the “Methods” chapter [Harris et al., 2013]). In general, thermal conductivity values in Hole U1381C

agree with values in Holes U1381A and U1381B using the same needle-probe method (Fig. F31A), and thermal conductivity results are inversely correlated with porosity (Fig. F27C). Thermal conductivity increases with depth to 50 mbsf, decreases slightly from 50 to 60 mbsf, and then gradually increases below 60 mbsf (Fig. F31A). The overall variation in thermal conductivity with depth is small, and the data yield a mean and standard deviation of 0.83 and 0.05 W/(m·K), respectively.

Downhole temperature and heat flow

Four downhole temperature measurements were attempted using the APCT-3 between 20 and 60 mbsf in Hole U1381C (Fig. F31B). All measurements were made in a calm sea state. The APCT-3 was stopped at the mudline for as long as 10 min prior to each penetration. Equilibrium temperature values plotted as a function of depth are relatively linear and show a similar trend with depth as Expedition 334 data. Coupled with the average bottom water temperature (2.4°C; Expedition 334 Scientists, 2012), they give a least-squares gradient of 231°C/km.

We calculate heat flow of 185 mW/m² as a product of the average thermal conductivity (0.83 W/[m·K]) and the thermal gradient. This value is significantly larger than the half-space prediction of 130 mW/m² for 15 Ma crust and much larger than the observed global average heat flow of 77 mW/m² for this age crust (Stein and Stein, 1994). This high heat flow suggests significant fluid flow in the underlying crust.

Sediment strength

Sediment strength was measured both by the automated vane shear (AVS) and the Geotester STCL-5 pocket penetrometer. To compare between the two measurements, unconfined shear strength is one half of unconfined compressive strength (Blum, 1997). Strength generally increases with depth. Expedition 334 data show much lower values than those from Expedition 344, probably because of disturbance from RCB coring during Expedition 334. The AVS and penetrometer measurements both show approximately linear trends within Unit I (Fig. F32). Values become scattered below 50 mbsf, and strengths measured by pocket penetrometer become more variable than those measured by vane shear. Strength values increase with depth to 85 mbsf, ranging between ~40 and ~110 kPa (vane shear) and between ~10 and ~340 kPa (compressive strength from penetrometer). Within the interval from 85 to 98 mbsf, shear strength decreases with depth, with a minimum value of ~30 kPa (vane shear) and ~120 kPa (compressive strength from penetrometer).

Below ~98 mbsf, values increase sharply with depth where calcareous clay (Unit III) and claystone (Unit IV) appear. Within Units III and IV, values increase as high as 145 kPa (vane shear) and 440 kPa (compressive strength from penetrometer).

Electrical conductivity and formation factor

Formation factor values were obtained from sediment conductivity measurements conducted in the γ - and z -axes of the split core (Fig. F33). The γ and z measurements are similar throughout the cored interval, indicating little anisotropy in electrical conductivity within the sediments. Within Unit I, electrical conductivity tends to decrease gradually with depth and ranges between 18 and 25 mS/cm. Within Unit II, values increase slightly, ranging between 19 and 26 mS/cm. Near 95 mbsf, conductivity reaches its highest value of 28 mS/cm. Formation factor ranges between 1.8 and 2.7 within Unit I and decreases slightly to 1.8–2.3 within Unit II. The transition seen at 58 mbsf may correspond with the boundary between silty clay (Unit I) and calcareous ooze (Unit II). The increasing conductivity trend at 95–100 mbsf corresponds with the start of calcareous clay (Unit III) and claystone (Unit IV).

Color spectrophotometry

Results from color reflectance measurements are presented in Figure F34. Reflectance L^* values vary between 30 and 50 throughout Hole U1381C. Reflectance a^* and b^* values show clear contrast between Units I and II. Reflectance a^* values in Unit I vary between ~2 and ~5, whereas in Units II–IV, values vary between 4 and 6. Reflectance b^* values vary between ~10 and ~5 in Unit I, whereas values in the units below Unit I scatter between ~10 and 0. Trends in color reflectance between 95 and 100 mbsf correspond with the start of calcareous clay (Unit III) and claystone (Unit IV). Within the basement (Unit V; basalt breccia), a^* values range between 6 and 9 and b^* values vary from ~20 to ~15.

Paleomagnetism

Cores 344-U1381C-1H through 12H were cored with the APC using two nonmagnetic cutting shoes. Core 344-U1381C-13X was cored with the XCB using a standard cutting shoe. Cores 1H through 9H were oriented with the FlexIT orientation tool. These crucial orientation data facilitate the magnetostratigraphy investigation for Hole U1381C. We made pass-through magnetometer measurements on all archive-half cores and on 85 discrete samples taken from the working halves. In order to isolate the characteristic remanent magnetization (ChRM), sedimentary archive-half

cores were demagnetized in an alternating field (AF) up to 30 mT and measured with the pass-through superconducting rock magnetometer (SRM) at 2.5 cm intervals.

Paleomagnetic discrete samples were subjected to stepwise AF demagnetization up to 120 or 200 mT and measured with the SRM. Paleomagnetic discrete samples were not taken from Cores 344-U1381C-12H and 13X because of the short pieces of the recovered core material.

Natural remanent magnetization of sedimentary cores

Downhole variations of paleomagnetic data obtained in Hole U1381C are shown in Figure F35. The variations in NRM intensity are correlated with lithology. Paleomagnetic measurements indicate that the silty clay in Unit I (0–55.93 mbsf) has a mean NRM intensity on the order of 10^{-2} A/m, whereas the foraminiferal nannofossil-rich calcareous ooze in Unit II has a much lower NRM intensity ($\sim 10^{-3}$ A/m). Many discrete peaks of higher NRM values that appear in some depth intervals in both Units I and II (e.g., ~8, ~26, and ~45 mbsf) can be tied directly to the presence of volcanic tephra in these layers (see “[Lithostratigraphy and petrology](#)”). Magnetic susceptibility data also show positive peaks at these intervals (see “[Physical properties](#)”).

Paleomagnetic demagnetization results

As with Hole U1381A cores recovered during Expedition 334, remagnetization imparted by the coring process was encountered in Hole U1381C. NRM inclinations are strongly biased toward the vertical (mostly toward $+90^\circ$) in a majority of cores. For the recovered sediment core sections, we employed AF demagnetization steps up to 30 mT at 5 mT increments. AF demagnetization to 5–10 mT seems to be effective in removing the drilling overprint magnetization, as shown by inclinations shifted toward shallower values that are comparable to the expected inclination for this site (approximately $\pm 17^\circ$) and by a factor of 3–4 decrease in magnetization intensity after 5 mT demagnetization and an order of magnitude decrease after 30 mT demagnetization (Fig. F35). For several core sections from Unit II, AF demagnetization up to 30 mT was not effective in recovering the primary remanence magnetization. Inclination shifts toward shallower values ($\sim 50^\circ$) but still seems to be dominated by the near-vertical drilling-induced remagnetization.

The NRM declinations of Cores 344-U1381C-1H through 9H before orientation correction are different from each other, as expected. Upon orientation

correction using the data from the FlexIT orientation tool, declinations are close to magnetic north for the normal polarity cores and magnetic south for some cores with negative inclinations, indicating the remanence is of geomagnetic origin (Fig. F35). More discussion about the magnetic declination records is given in “[Magnetostratigraphy](#),” below.

The magnetic properties observed from the section halves were also confirmed by discrete sample measurements (Fig. F36). The nearly vertical overprint was removed by AF demagnetization of 5–10 mT for nearly all the samples. AF demagnetization was generally successful in isolating ChRM for most discrete samples: 58 out of 85 tested samples revealed ChRM with maximum angular dispersion $<15^\circ$. Most discrete samples in Unit I show straightforward demagnetization behavior and reveal the ChRM. Several discrete samples from the lower part of Unit II, however, display more complicated demagnetization paths that do not decay simply toward the origin. An intermediate component with negative inclination but northerly declination is exhibited in these samples, which may be constrained by the great circles method. A small portion of samples also displayed erratic or incoherent demagnetization behavior, with data points that could not be fit to a line using the principal component analysis method (Kirschvink, 1980).

Magnetostratigraphy

We used ChRM declinations and inclinations from discrete measurements to define magnetic polarity sequences for the oriented cores in Hole U1381C. At a low-latitude area such as the location of Site U1381, a near 180° shift in declination in the cores is a more reliable sign of a polarity reversal than a change in sign of inclination.

As shown in Figure F37, several magnetic reversals were discerned on the basis of changes in sign of both inclinations and declinations. Based on a tephra layer that is present at ~25 mbsf and is believed to be the Tiribi Tuff ash layer (Ar-Ar dated at 320 ± 2 ka; Pérez et al., 2006), the two possibly reversed polarity zones in the depth interval from ~16 to 19 mbsf (Sections 344-U1381C-2H-6 through 3H-2) are tentatively identified as Subchrons Biwa I (176–186 ka) and Biwa II (292–298 ka) (Kawai et al., 1972). Shipboard micropaleontological studies also suggest that Core 2H should be older than 120 ka. The Brunhes/Matuyama Chron boundary (0.78 Ma) is tentatively placed at ~49 mbsf between Section 344-U1381C-6H-3, 5 cm (49.2 mbsf), and 6H-3, 83 cm (49.98 mbsf). Lower Pleistocene biostratigraphic Zone NN19 is also placed in this interval (see “[Paleontology and biostratigraphy](#)”).

Below the Brunhes/Matuyama Chron boundary, although the directional record defines several normal and reversed polarity zones, only one relatively well defined polarity interval has been identified in the downhole magnetostratigraphic records at ~61–64 mbsf (Fig. F37). Small magnetic polarity changes after the Brunhes/Matuyama Chron boundary were recently documented (e.g., Jovane et al., 2008; Suganuma et al., 2011). Some of these small inclination fluctuations in Figure F37 may correspond to such changes. From Section 344-U1381C-7H-7 through the top part of Section 10H-5, negative inclinations are dominant, consistent with the notion that these cores were magnetized in a reversed field. The corresponding declinations, however, are close to magnetic north, suggesting that these cores may have recorded a normal polarity. More detailed postcruise paleomagnetic studies are needed to resolve the polarity assignment and improve the magnetostratigraphy at Site U1381.

Shipboard lithologic and micropaleontological studies suggest that sediments in Cores 344-U1381C-7H through 11H have ages 9–14 Ma, inferring a ~9 m.y. hiatus between Cores 6H and 7H. If correct, the mixed polarity sequence extending from 56 to 103 mbsf (Fig. F37) should be within Chrons C5–C5AA in the middle Miocene (Stages Tortonian–Serravalian; 11.63–15.16 Ma).

References

- Barckhausen, U., Ranero, C.R., von Huene, R., Cande, S.C., and Roeser, H.A., 2001. Revised tectonic boundaries in the Cocos plate off Costa Rica: implications for the segmentation of the convergent margin and for plate tectonic models. *J. Geophys. Res.: Solid Earth*, 106(B9):19207–19220. doi:10.1029/2001JB000238
- Blum, P., 1997. Physical properties handbook: a guide to the shipboard measurement of physical properties of deep-sea cores. *ODP Tech. Note*, 26. doi:10.2973/odp.tn.26.1997
- Carey, S., 1997. Influence of convective sedimentation on the formation of widespread tephra fall layers in the deep sea. *Geology*, 25(9):839–842. doi:10.1130/0091-7613(1997)025<0839:IOCSOT>2.3.CO;2
- Corliss, B.H., 1985. Microhabitats of benthic foraminifera within deep-sea sediments. *Nature (London, U. K.)*, 314(6010):435–438. doi:10.1038/314435a0
- Expedition 334 Scientists, 2012. Site U1381. In Vannucchi, P., Ujiie, K., Stroncik, N., Malinverno, A., and the Expedition 334 Scientists, *Proc. IODP*, 334: Tokyo (Integrated Ocean Drilling Program Management International, Inc.). doi:10.2204/iodp.proc.334.106.2012
- Harris, R.N., Sakaguchi, A., Petronotis, K., Baxter, A.T., Berg, R., Burkett, A., Charpentier, D., Choi, J., Diz Ferrero, P., Hamahashi, M., Hashimoto, Y., Heydolph, K., Jovane, L., Kastner, M., Kurz, W., Kutterolf, S.O., Li, Y., Malinverno, A., Martin, K.M., Millan, C., Nascimento, D.B., Saito, S., Sandoval Gutierrez, M.I., Sreaton, E.J., Smith-Duque, C.E., Solomon, E.A., Straub, S.M., Tanikawa, W., Torres, M.E., Uchimura, H., Vannucchi, P., Yamamoto, Y., Yan, Q., and Zhao, X., 2013. Methods. In Harris, R.N., Sakaguchi, A., Petronotis, K., and the Expedition 334 Scientists, *Proc IODP*, 344: College Station, TX (Integrated Ocean Drilling Program). doi:10.2204/iodp.proc.344.102.2013
- Gooday, A.J., and Rathburn, A.E., 1999. Temporal variability in living deep-sea benthic foraminifera: a review. *Earth Sci. Rev.*, 46(1–4):187–212. doi:10.1016/S0012-8252(99)00010-0
- Hayward, B.W., 2002. Late Pliocene to middle Pleistocene extinctions of deep-sea benthic foraminifera (“*Stilostomella* extinction”) in the southwest Pacific. *J. Foraminiferal Res.*, 32(3):274–307. doi:10.2113/32.3.274
- Jovane, L., Acton, G., Florindo, F., and Verosub, K.L., 2008. Geomagnetic field behavior at high latitudes from a paleomagnetic record from Eltanin Core 27–21 in the Ross Sea sector, Antarctica. *Earth Planet. Sci. Lett.*, 267(3–4):435–443. doi:10.1016/j.epsl.2007.12.006
- Kawai, N., Yaskawa, K., Nakajima, T., Torii, M., and Horie, S., 1972. Oscillating geomagnetic field with a recurring reversal discovered from Lake Biwa. *Proc. Jpn. Acad.*, 48:186–190.
- Kimura, G., Silver, E.A., Blum, P., et al., 1997. *Proc. ODP, Init. Repts.*, 170: College Station, TX (Ocean Drilling Program). doi:10.2973/odp.proc.ir.170.1997
- Kirschvink, J.L., 1980. The least-squares line and plane and the analysis of palaeomagnetic data. *Geophys. J. R. Astron. Soc.*, 62(3):699–718. doi:10.1111/j.1365-246X.1980.tb02601.x
- Pérez, W., Alvarado, G.E., and Gans, P.B., 2006. The 322 ka Tiribí Tuff: stratigraphy, geochronology, and mechanisms of deposition of the largest and most recent ignimbrite in the Valle Central, Costa Rica. *Bull. Volcanol.*, 69(1):25–40. doi:10.1007/s00445-006-0053-x
- Sanfilippo, A., and Nigrini, C., 1998. Code numbers for Cenozoic low latitude radiolarian biostratigraphic zones and GPTS conversion tables. *Mar. Micropaleontol.*, 33(1–2):109–117, 121–156. doi:10.1016/S0377-8398(97)00030-3
- Stein, C.A., and Stein, S., 1994. Constraints on hydrothermal heat flux through the oceanic lithosphere from global heat flow. *J. Geophys. Res.: Solid Earth*, 99(B2):3081–3095. doi:10.1029/93JB02222
- Suganuma, Y., Okuno, J., Heslop, D., Roberts, A.P., Yamazaki, T., and Yokoyama, Y., 2011. Post-depositional remanent magnetization lock-in for marine sediments deduced from ¹⁰Be and paleomagnetic records through the Matuyama–Brunhes boundary. *Earth Planet. Sci. Lett.*, 311(1–2):39–52. doi:10.1016/j.epsl.2011.08.038
- Zijderveld, J.D.A., 1967. AC demagnetization of rocks: analysis of results. In Collinson, D.W., Creer, K.M., and Runcorn, S.K. (Eds.), *Methods in Palaeomagnetism*: Amsterdam (Elsevier), 254–286.

Publication: 11 December 2013
MS 344-103

Figure F1. Detail of prestack time-migrated seismic Line BGR99-7 centered at Site U1381. Prestack depth migration from C.R. Ranero (unpubl. data).

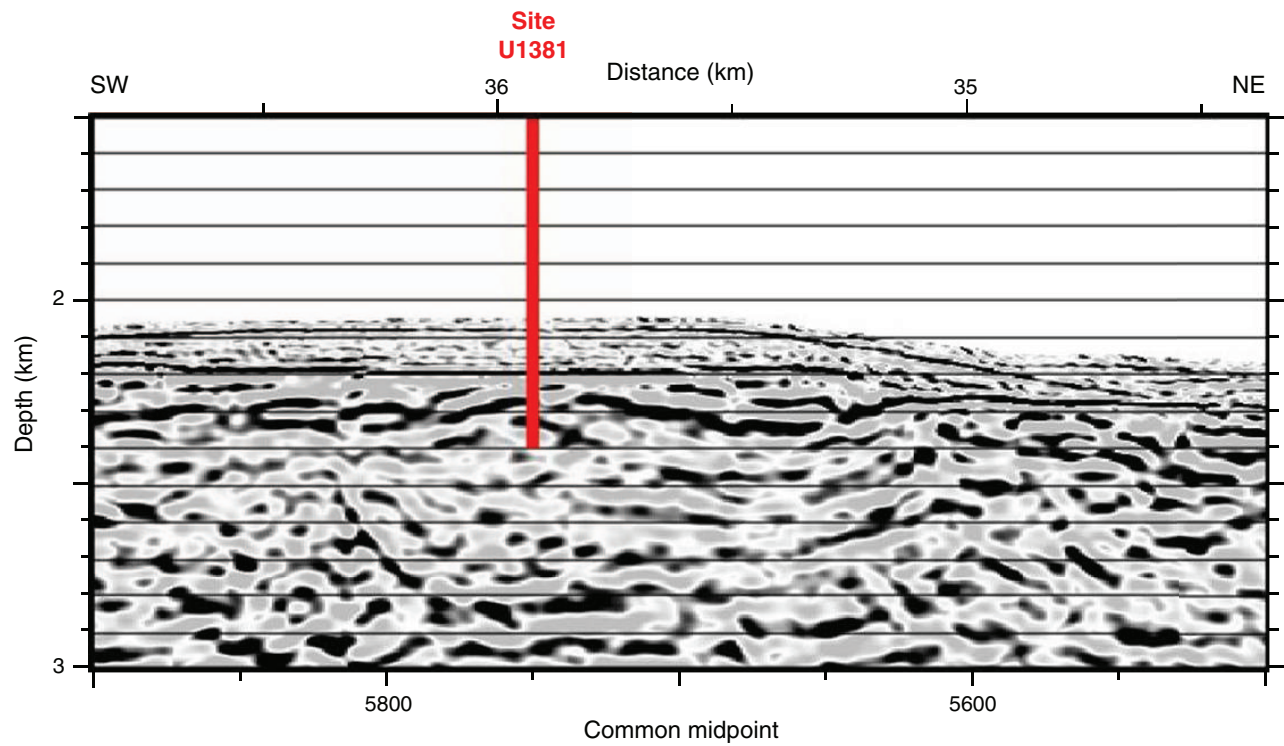


Figure F2. Location of Expedition 344 drill sites. Red diamonds denote Expedition 344 sites (U1380, U1381, and U1412–U1414), and yellow diamonds denote Expedition 334 sites not occupied during Expedition 344 (Sites U1378 and U1379). Red lines = 3-D seismic survey, black lines = seismic reflection lines. Numbers along the short and long axes of the 3-D survey represent inlines and crosslines, respectively.

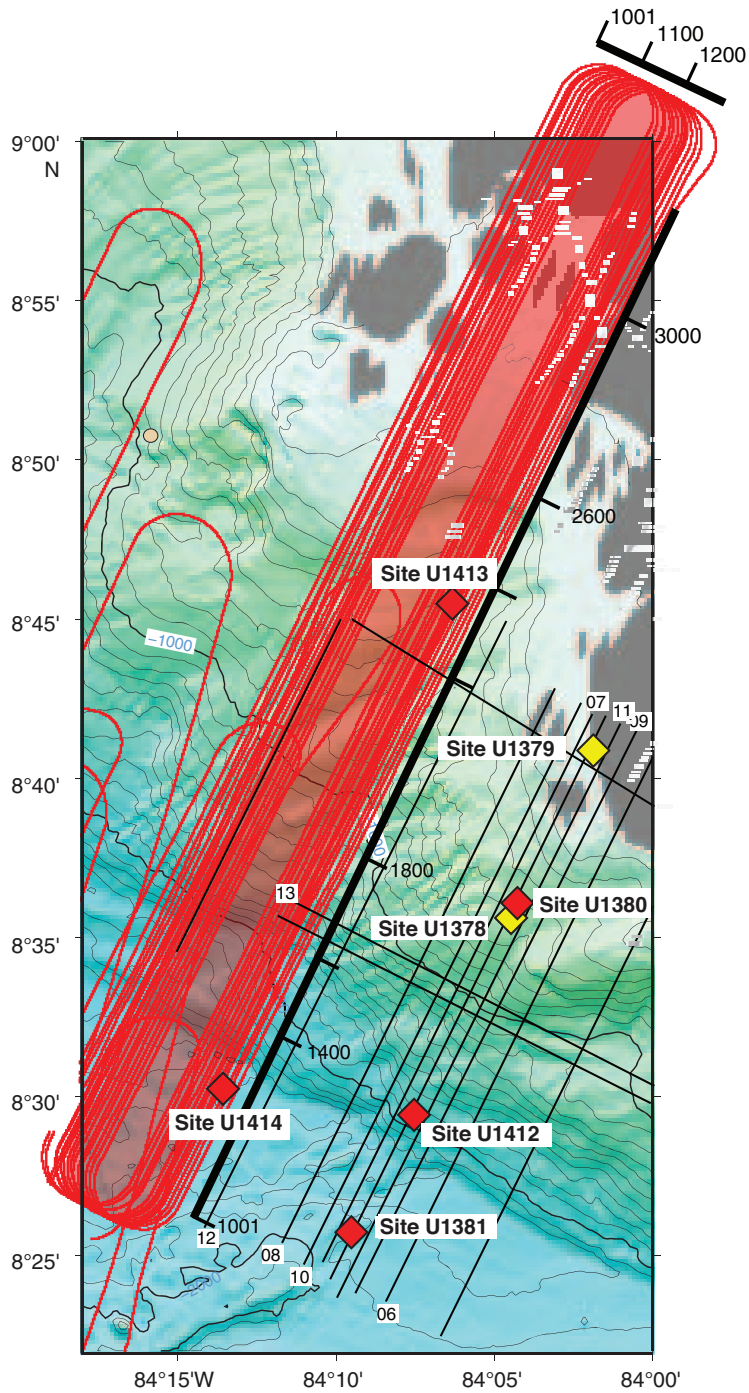


Figure F3. Lithostratigraphic summary of Hole U1381C.

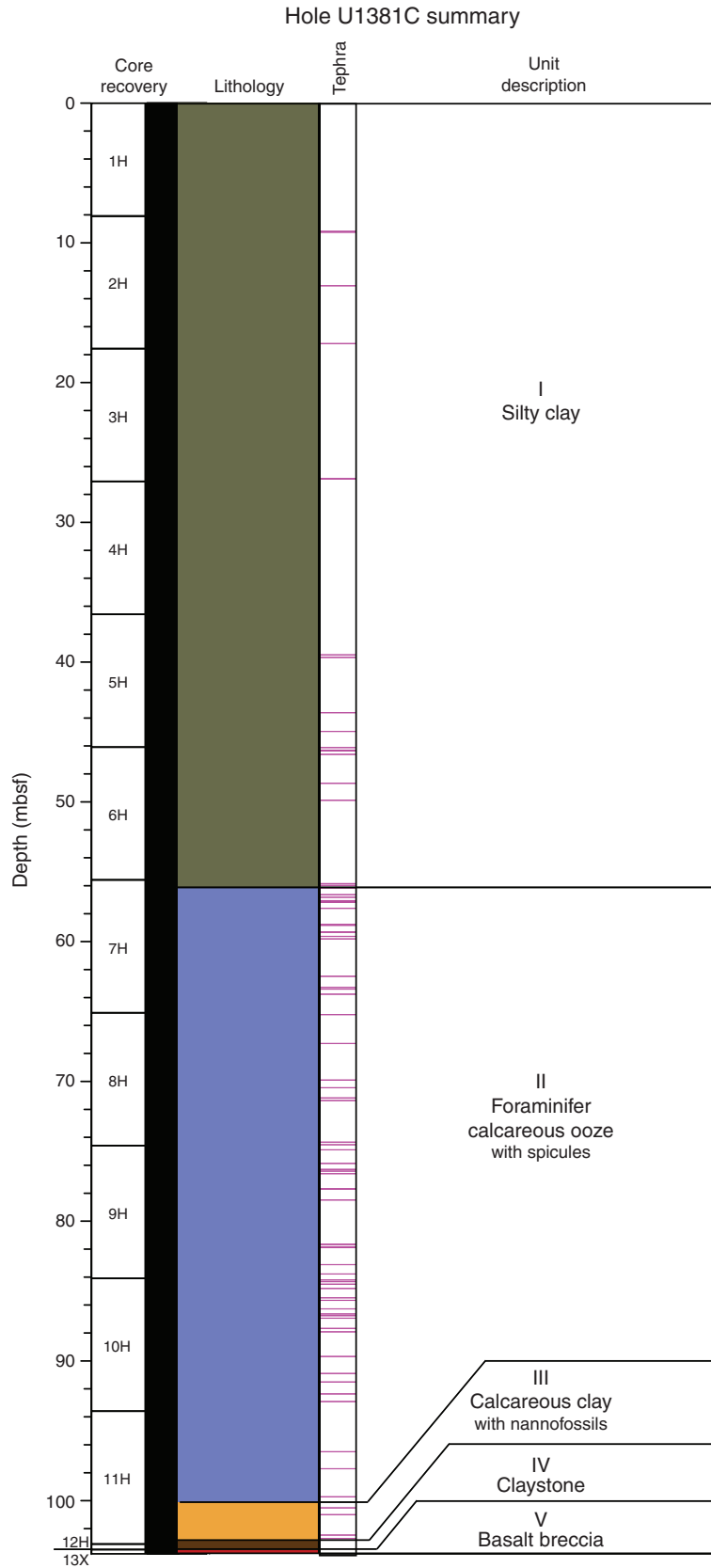


Figure F4. Representative digital image of lithostratigraphic Unit I; grayish green massive silty clay with common tephra lenses, pyrite smudges, and pyrite-rimmed burrows (interval 344-U1381C-3H-7A, 27–57 cm).

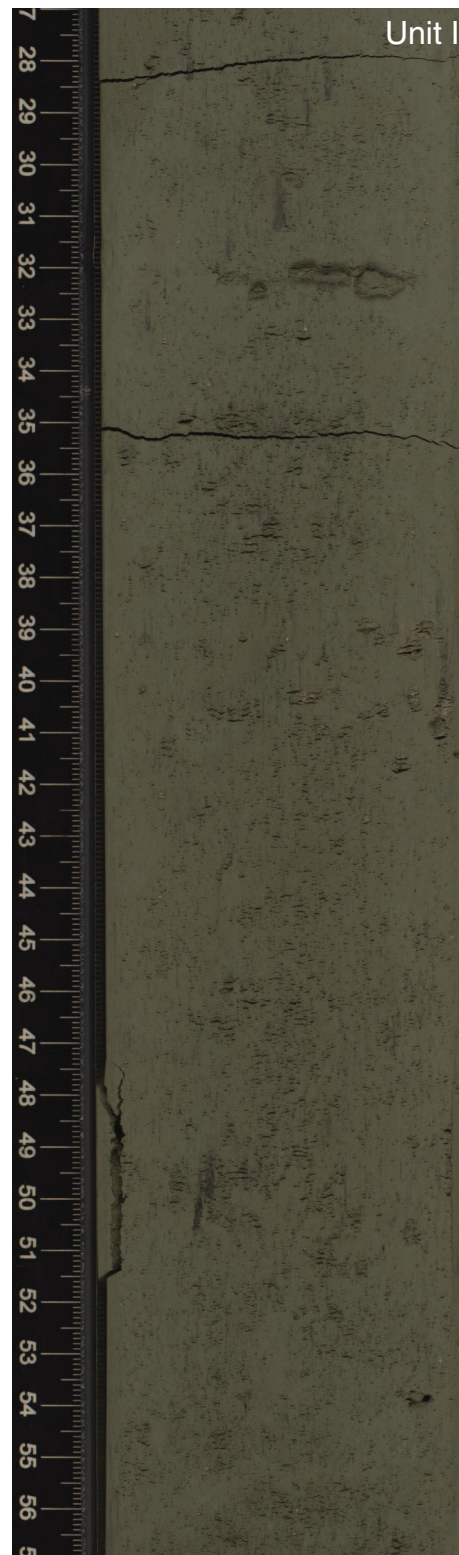


Figure F5. Digital image of a ~3.5 cm thick pinkish gray felsic tephra layer at 72.5–76 cm (interval 344-U1381C-5H-6A, 66–81 cm). Contact is sharp at the base, with medium sand-sized ash that grades upward into a fine silt-sized ash.



Figure F6. Digital image of a slightly consolidated tephra layer with dark minerals enriched at the base and associated bioturbated tephra lenses at 14.5–20 cm (interval 344-U1381C-3H-7A, 11–26 cm). Tephra varies from pinkish gray to medium gray and is made of coarse to medium sand-sized ash with normal grading.



Figure F7. Digital image of the lithologic boundary (dashed white line) between Units I and II (interval 344-U1381C-7H-1A, 26–56 cm). Unit II is grayish brown massive silty nannofossil ooze with abundant tephra layers that are often bioturbated.



Figure F8. Digital image of very dark gray lithified tephra layer with an inclined, well-defined, sharp boundary at the bottom at ~49 cm (interval 344-U1381C-7H-2A, 1–55 cm). Grain sizes show gradation from fine sand at the base to medium silt toward the top. Smearred edges are caused by drilling disturbance.



Figure F9. Digital image of two very dark gray, normally graded tephra layers between 52 and 70 cm that are moderately consolidated to lithified and exhibit slight bioturbation (interval 344-U1381C-7H-3A, 49–74 cm). Ash sizes vary from medium and fine sand at the base to silt and clay-sized ash toward the top.



Figure F10. Digital image of the lithologic boundary (dashed white line) between Units II and III, massive clayey carbonaceous ooze containing mineral-filled veins and deformation bands (interval 344-U1381C-11H-5A, 94–115 cm).

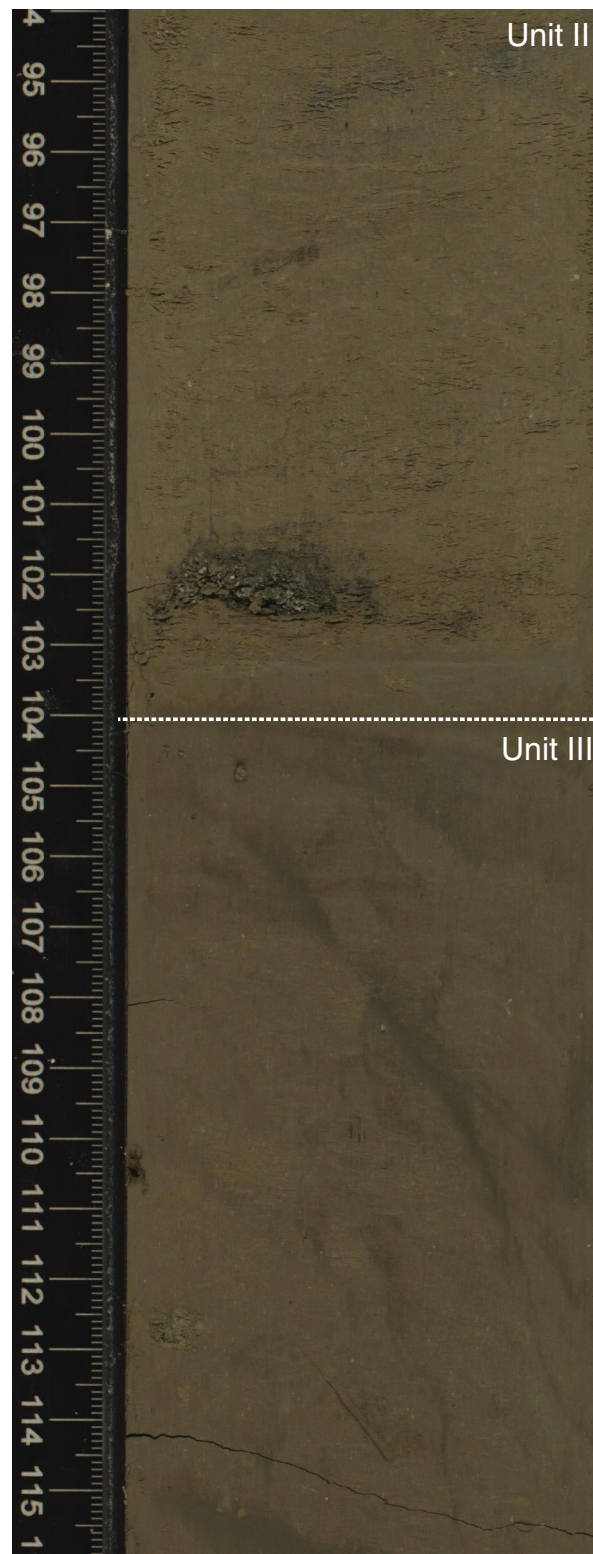


Figure F11. Digital image of Unit III/ IV boundary (interval 344-U1381C-12H-1A, 0–27 cm). Unit IV consists of grayish black claystone with some interlayered clay almost completely devoid of biogenic components. High degree of fragmentation is due to drilling disturbance.



Figure F12. Digital image of Unit V, which comprises a poorly sorted fractured basaltic breccia composed of variably disturbed altered basaltic matrix and basaltic clasts that are partly to completely coated in pyrite (interval 344-U1381C-13X-1A, 0–32 cm).



Figure F13. Typical XRD patterns obtained for bulk rock samples, Hole U1381C. A = amphibole (hornblende), Al = albite (Ca rich), An = anhydrite, B = biotite, C = calcite, Chl = chlorite (clinochlore), H = halite, P = pyroxene, Py = pyrite, Q = quartz, S = smectite, Z = zeolites (laumontite and stilbite in Unit I; heulandite in Unit III).

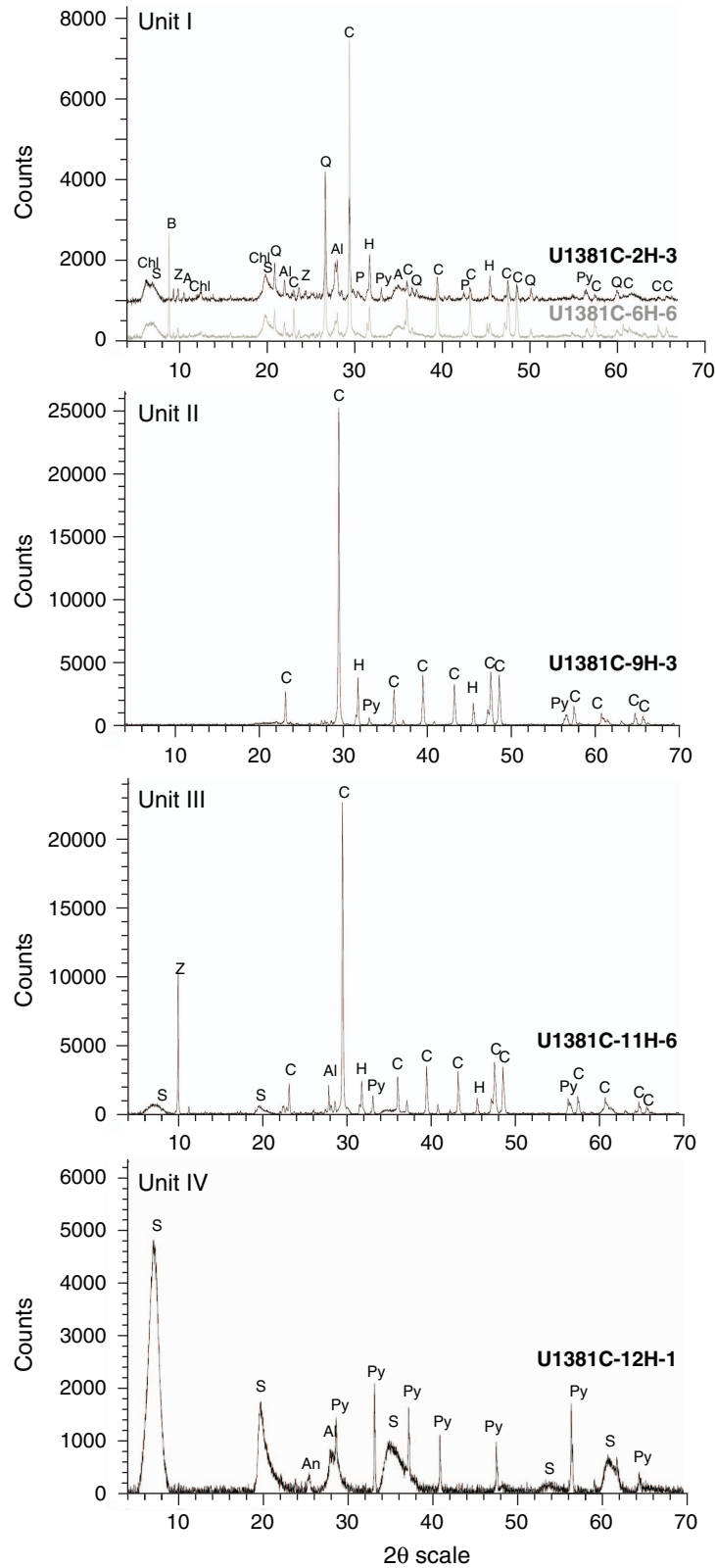


Figure F15. Plate showing biostratigraphically important radiolarian species, Hole U1381C. **A.** Unit I. 1. *Didymocyrtis tetralthalamus*. 2. *Amphirhopalum angulare*. 3. *Anthocyrtidium* sp. 4. *Botryostrobos auritus*. 5. *Dictyophimus infabricatus*. 6. *Neophrosipyris renilla*. 7. *Spongaster tetra*. 8. *Dictyocorne* sp. 9. *Zygocircus productus*. **B.** Unit II. 1. *Didymocyrtis violina*. 2. *Didymocyrtis laticonus*. 3. *Cryptocapsella cornuta*. 4. *Cryptocapsella tetrapera*. 5. *Lithopera renzae*. 6. *Stichocorys armata*. 7. *Spyrocyrtis subtilis*. 8. *Liriospyris parkerae*. 9. *Trisolenia megalactis costlowi*. 10. *Periphaena decora*.

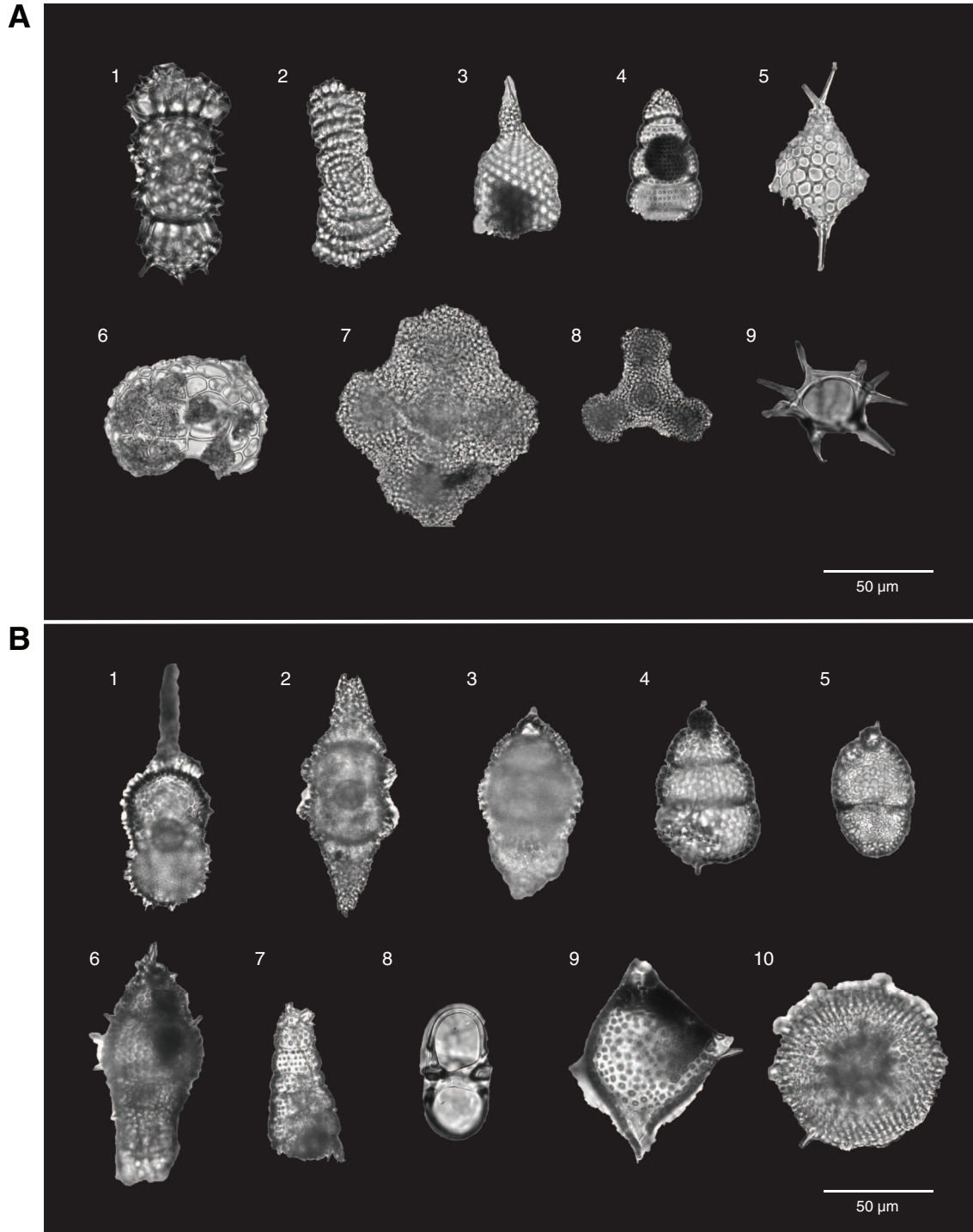




Figure F16. Benthic foraminifer assemblage changes between the upper and lower portions of Hole U1381C.

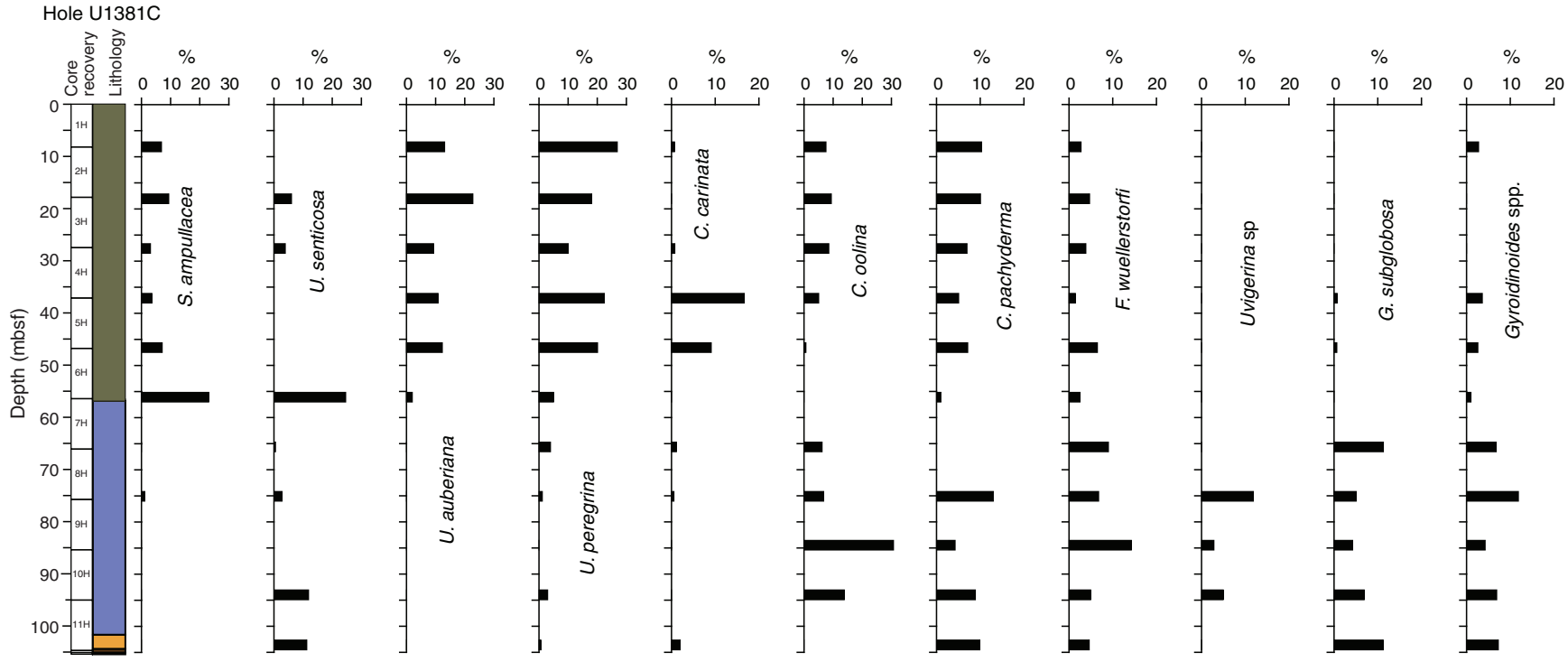


Figure F17. Plot of bedding dips, fractures, faults, and mineral-filled veins as a function of depth, Hole U1381C. Horizontal lines = lithostratigraphic unit boundaries.

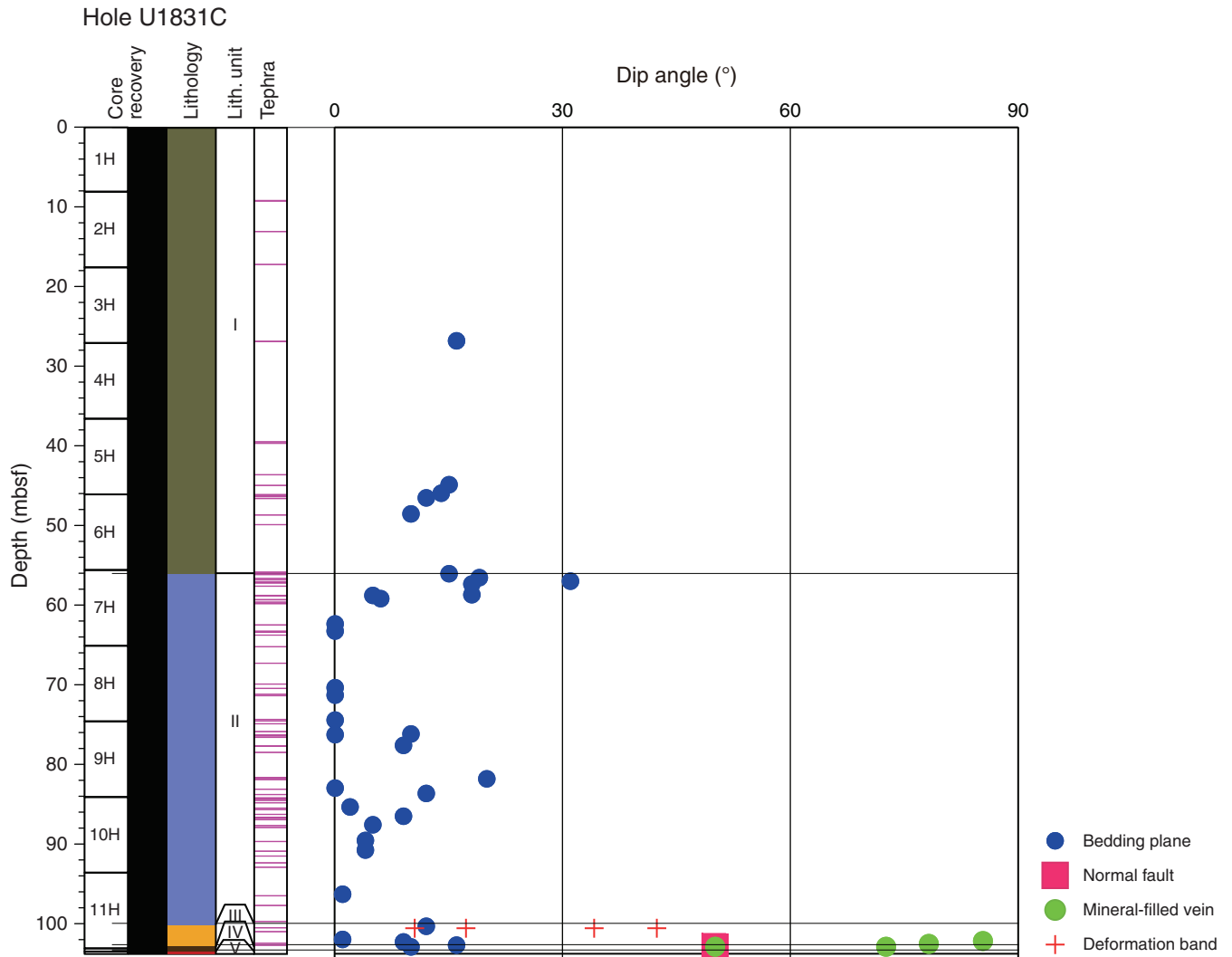


Figure F18. Stereographic diagrams showing orientation data of bedding planes from Units I and II, Hole U1381C.

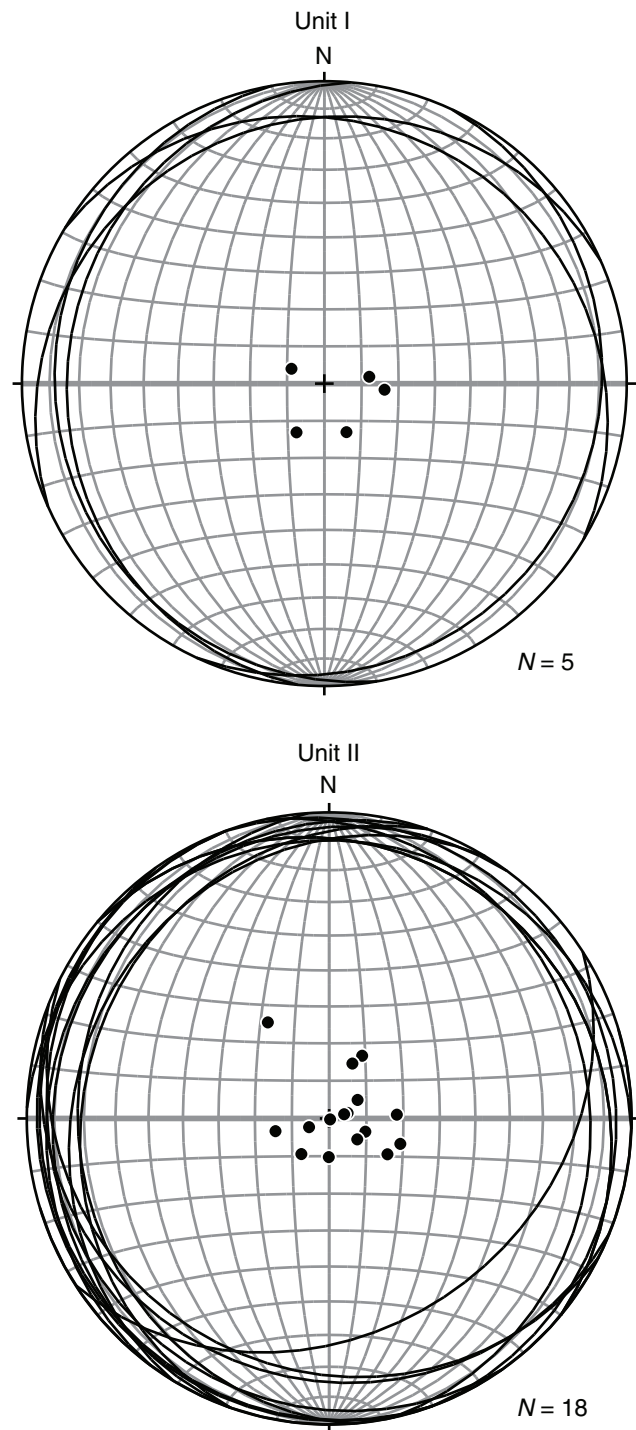
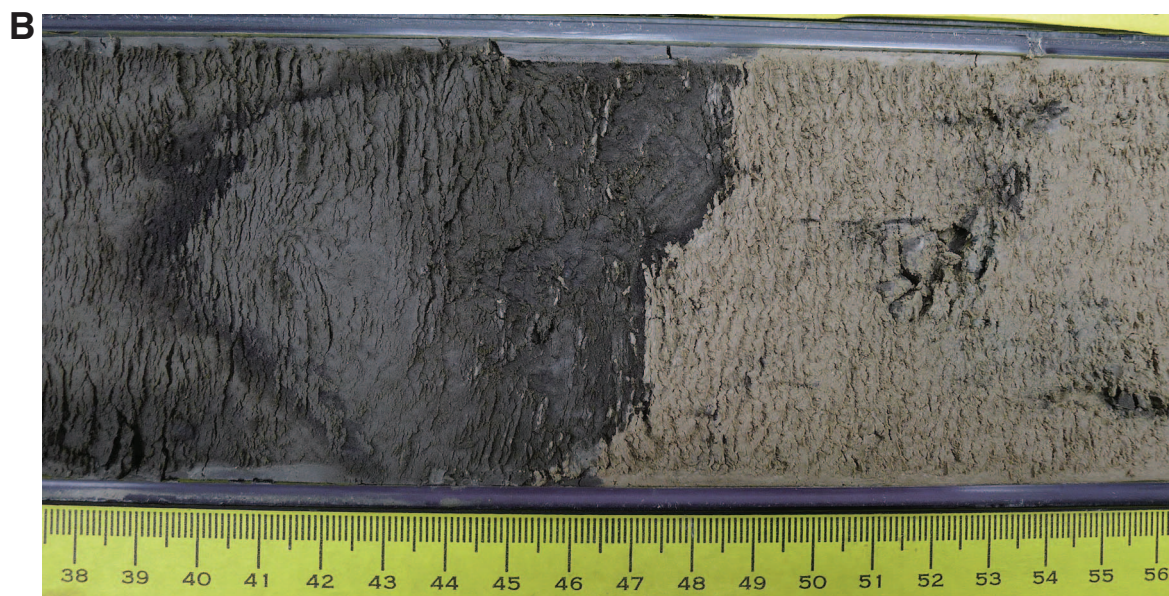


Figure F19. Core photographs. A. Photograph of Core 344-U1381C-7H (archive half). B. Photograph of tephra layer (dark colored) with fine-grained clastic sediment (interval 344-U1381C-7H-2W, 38–56 cm). Contacts are characterized by sharp scoured bases.



← Top



← Top

Figure F20. Core photographs. A. Photograph of deformation bands (interval 344-U1381C-11H-5W, 103–119 cm). B. Photograph of mineral-filled veins (zeolite and smectite) (interval 344-U1381C-11H-7W, 7–30 cm).



Figure F21. Stereographic diagrams with orientation data of mineralized shear fractures and veins from Unit III, lower hemisphere projection, Hole U1381C.

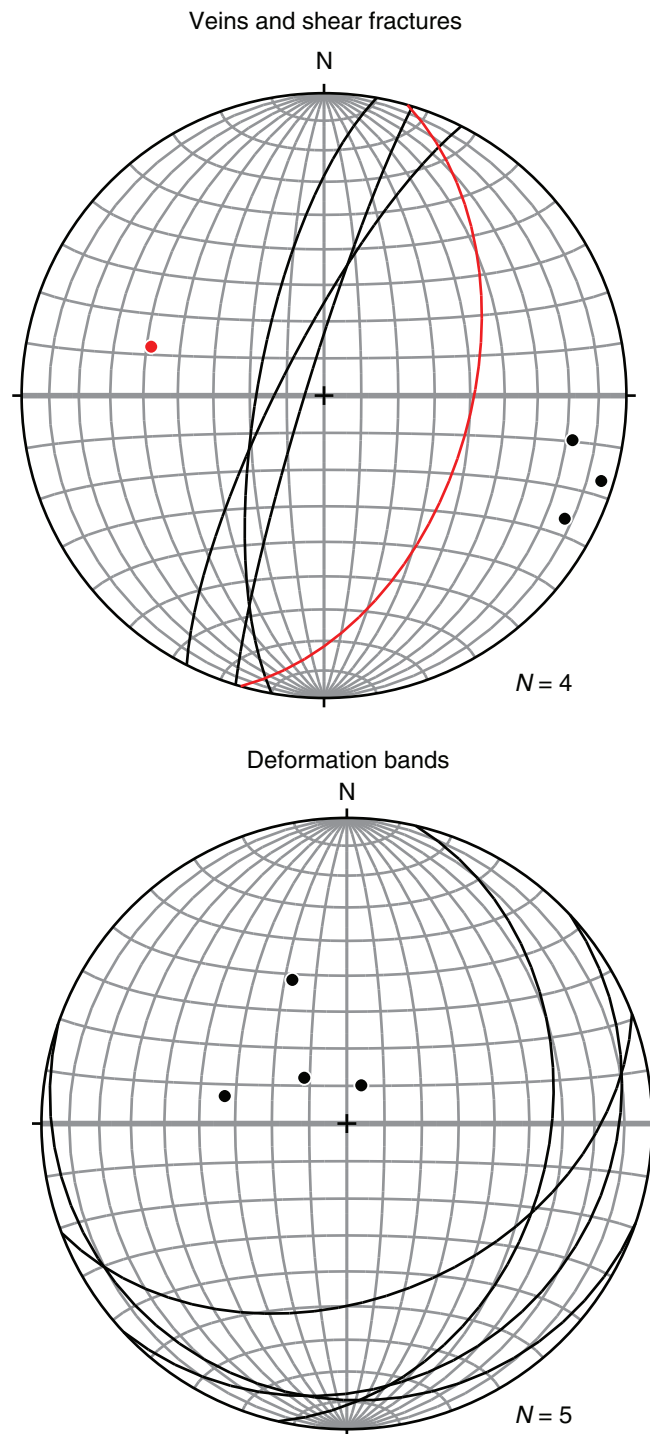


Figure F22. Downhole profiles of salinity, chloride, sodium, and potassium, Hole U1381C. Data collected in Hole U1381B during Expedition 334 (Expedition 334 Scientists, 2012) are shown for comparison. Blue arrows = bottom seawater values. Dashed lines = lithostratigraphic unit boundaries.

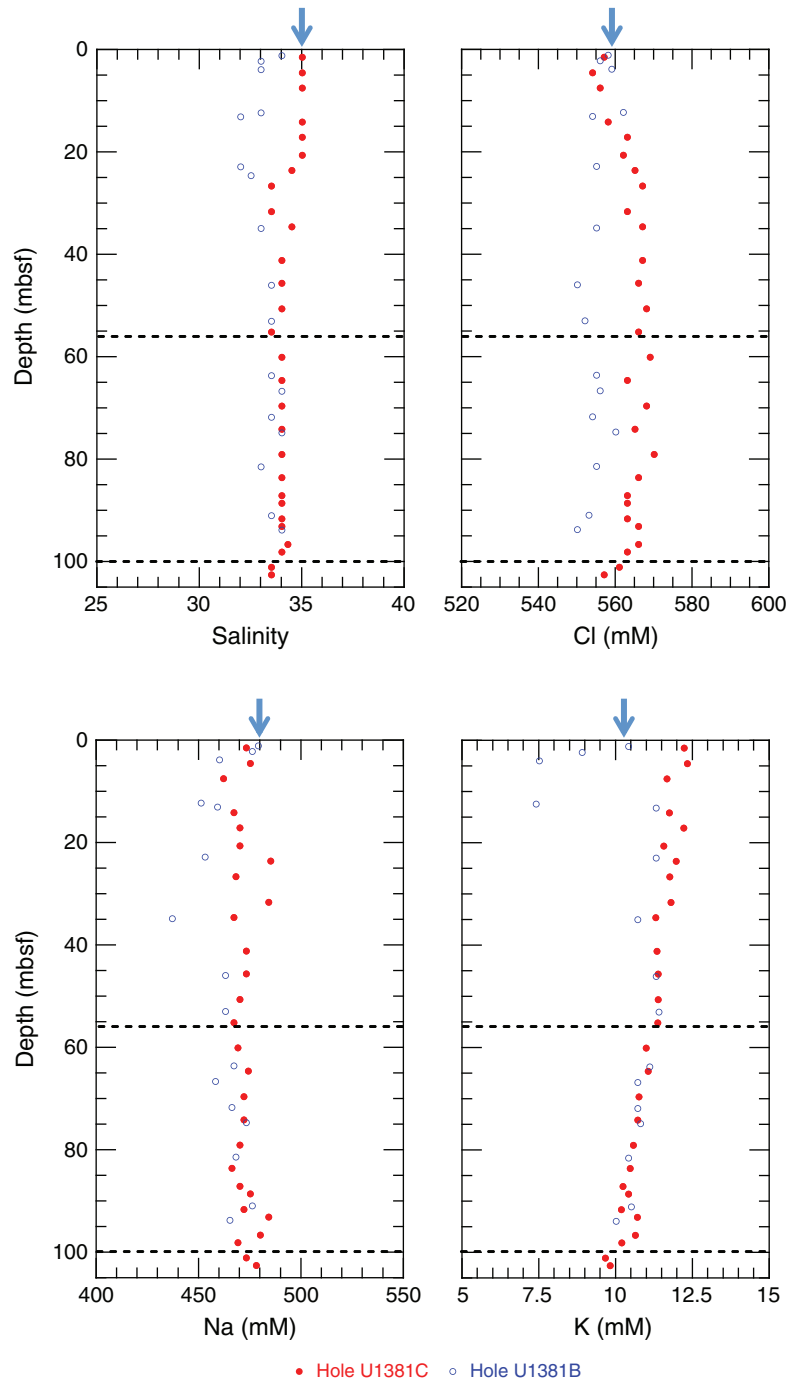


Figure F23. Downhole profiles of alkalinity, sulfate, ammonium, calcium, magnesium and phosphate, Hole U1381C. Data collected in Hole U1381B during Expedition 334 (Expedition 334 Scientists, 2012) are shown for comparison. Blue arrows = bottom seawater values. Dashed lines = lithostratigraphic unit boundaries.

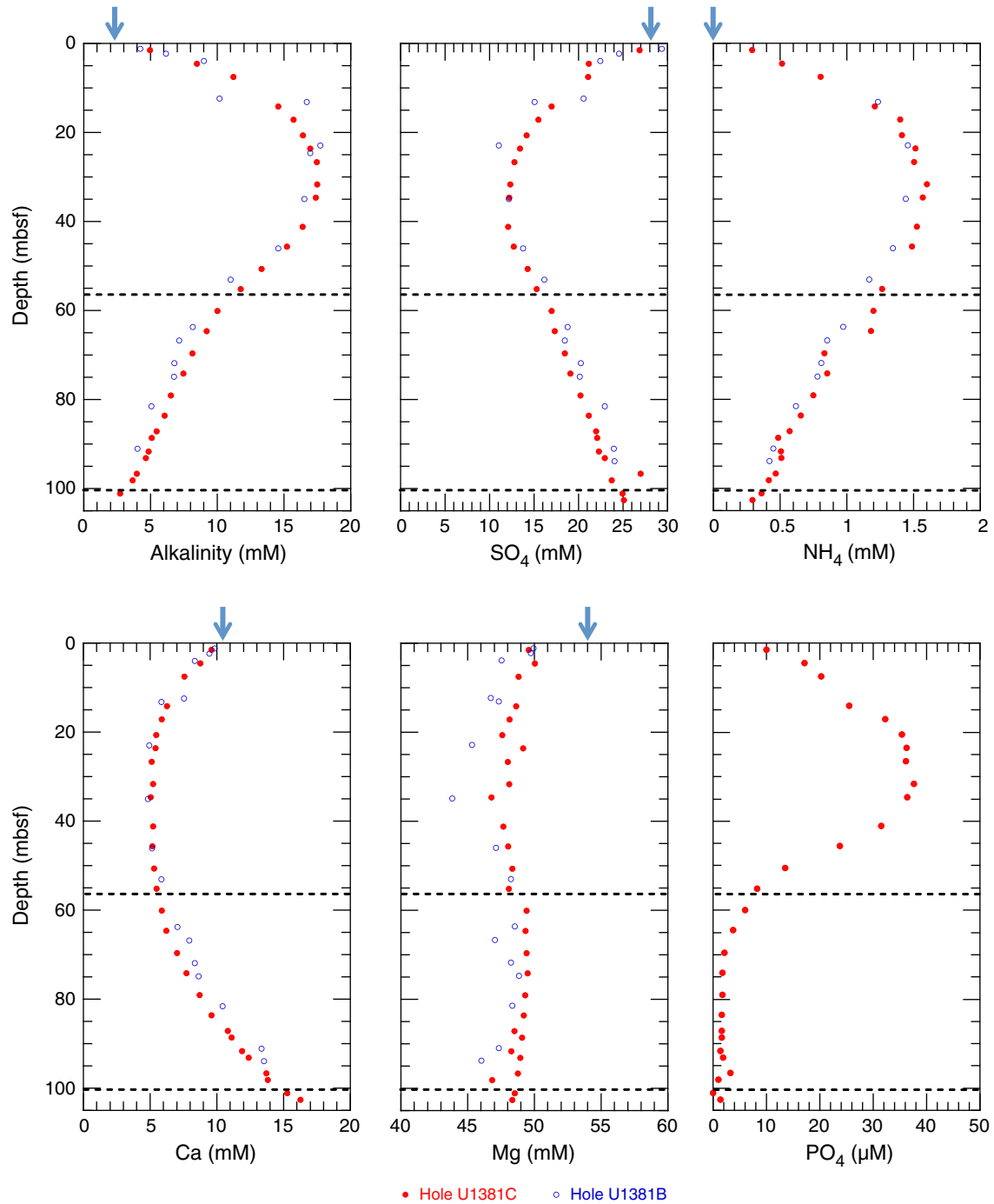


Figure F24. Downhole profiles of strontium, lithium, manganese, silica, boron, and barium, Hole U1381C. Data from samples collected in Hole U1381B during Expedition 334 (M.E. Torres et al., unpubl. data) are shown for comparison. Blue arrows = bottom seawater values. Dashed lines = lithostratigraphic unit boundaries.

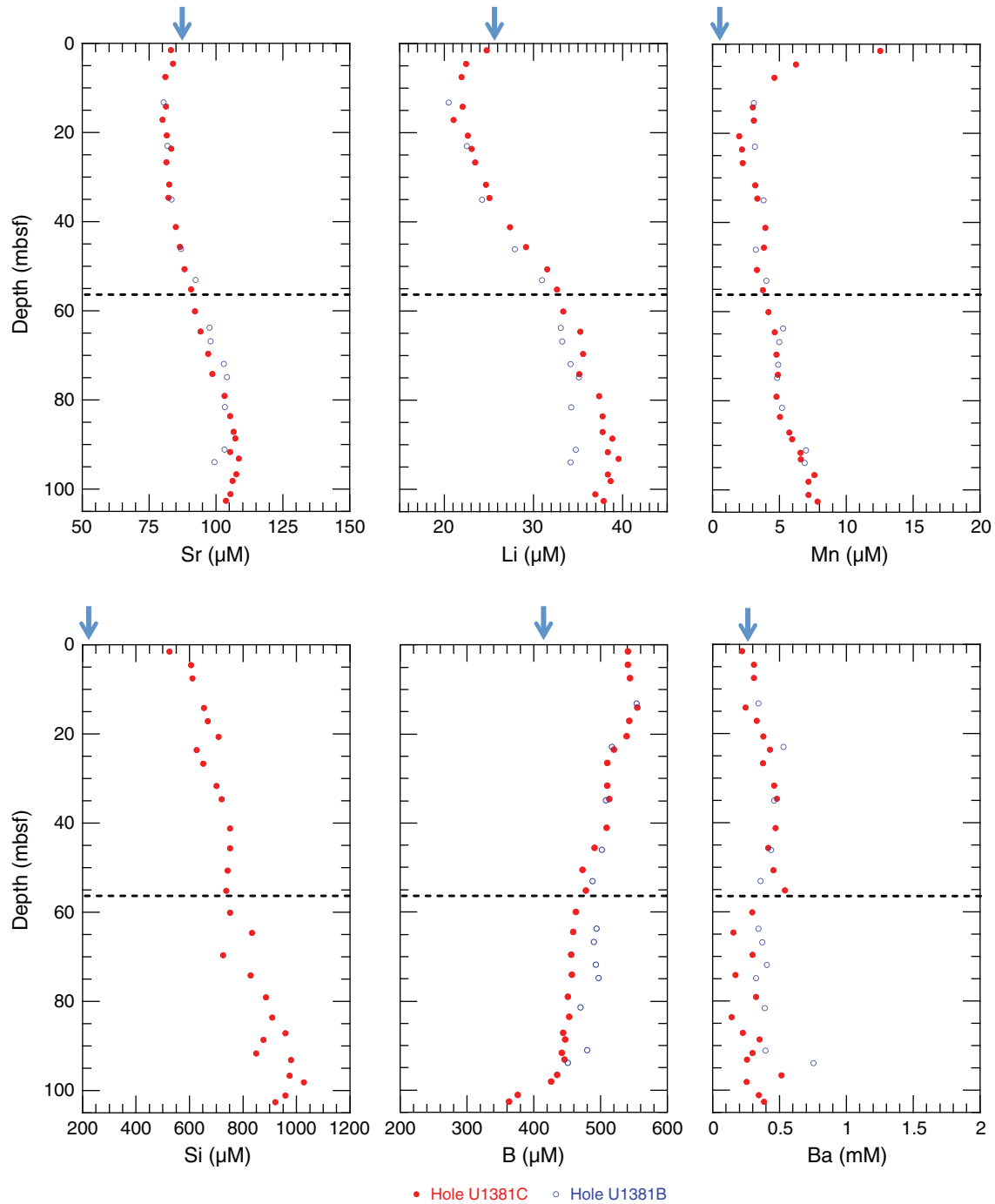


Figure F25. Downhole profile of methane in headspace gas, Hole U1381C. Dashed lines = lithostratigraphic unit boundaries.

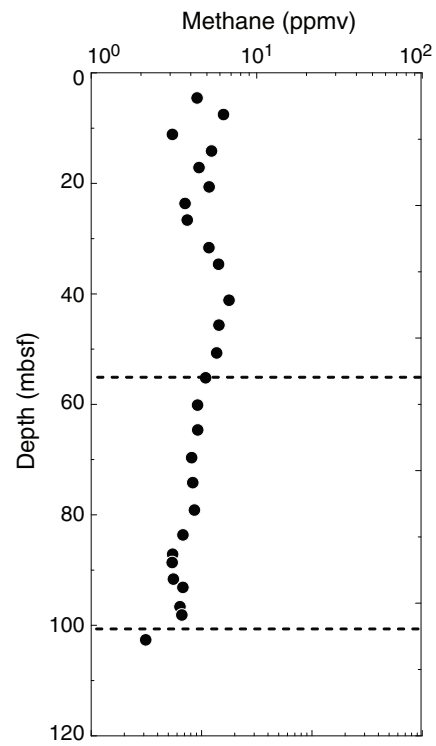


Figure F26. Downhole profiles of CaCO_3 , inorganic carbon, total organic carbon, and total nitrogen, Hole U1381C. Dashed lines = lithostratigraphic unit boundaries.

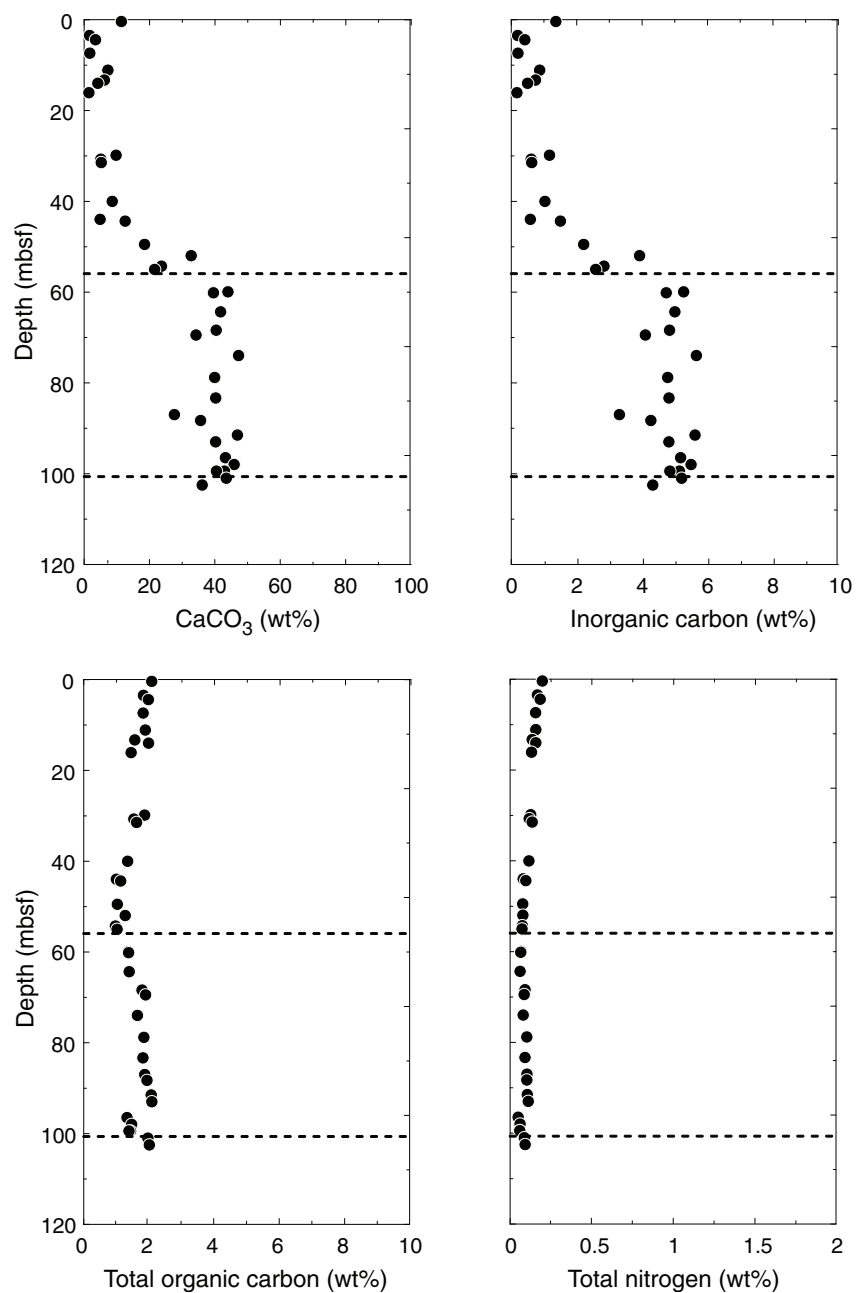


Figure F27. Gamma ray attenuation (GRA) density from the Whole-Round Multisensor Logger (WRMSL) and discrete sample porosity and density using moisture and density (MAD) mass/volume Method C, Site U1381. Horizontal lines = lithostratigraphic unit boundaries. **A.** GRA density and wet bulk density. **B.** Grain density. **C.** Porosity.

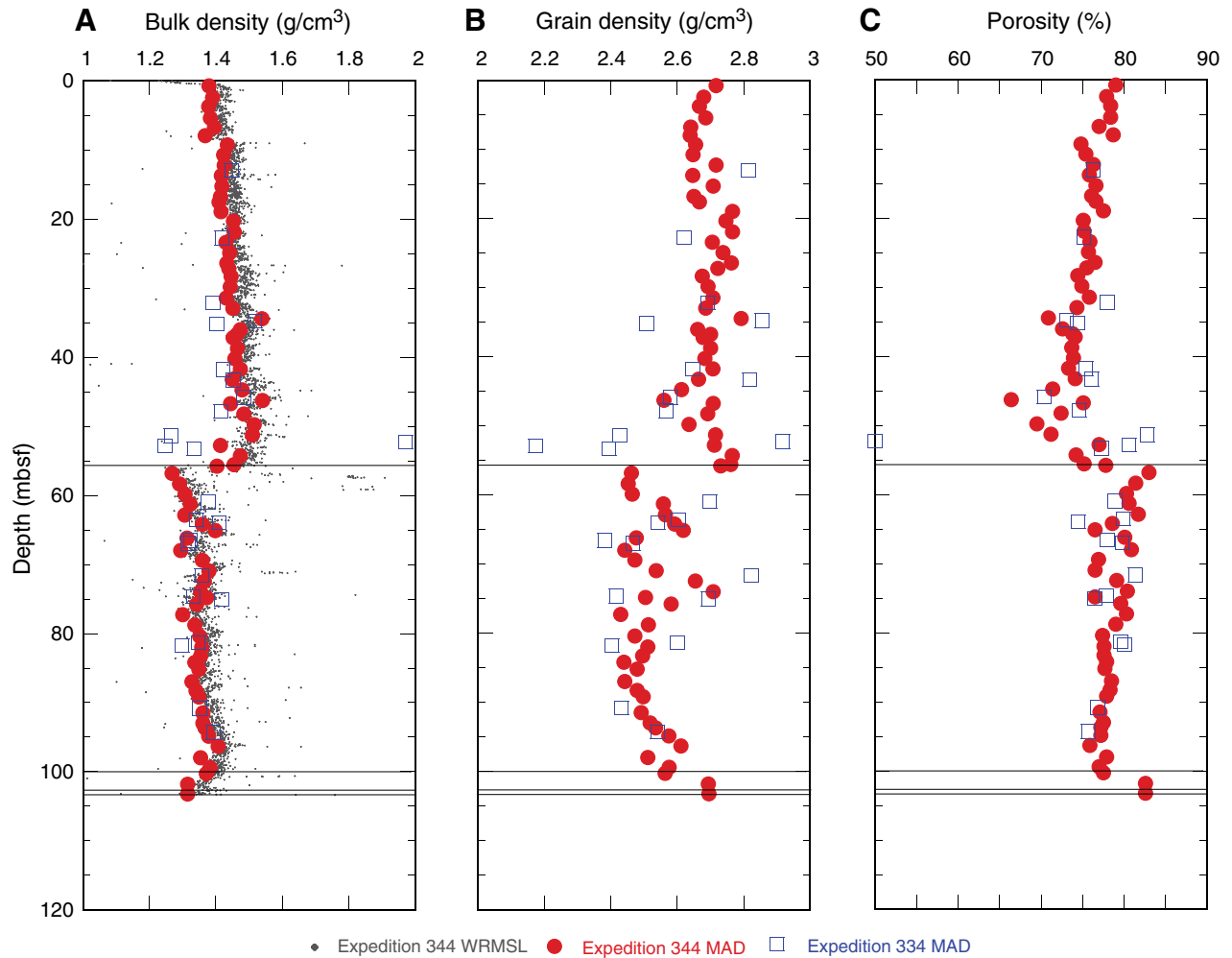


Figure F28. Magnetic susceptibility profiles, Site U1381. WRMSL = Whole-Round Multisensor Logger, SHMSL = Section Half Multisensor Logger. Horizontal lines = lithostratigraphic unit boundaries.

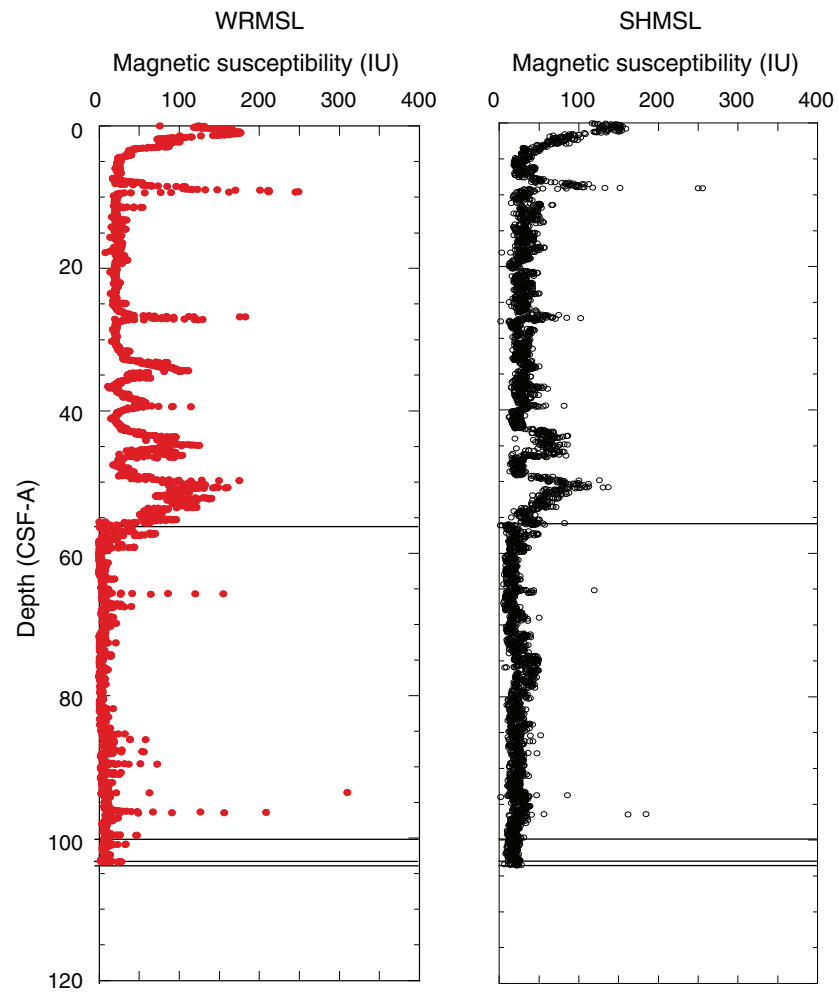


Figure F29. Downhole profile for natural gamma radiation (NGR), Site U1381. Horizontal lines = lithostratigraphic unit boundaries.

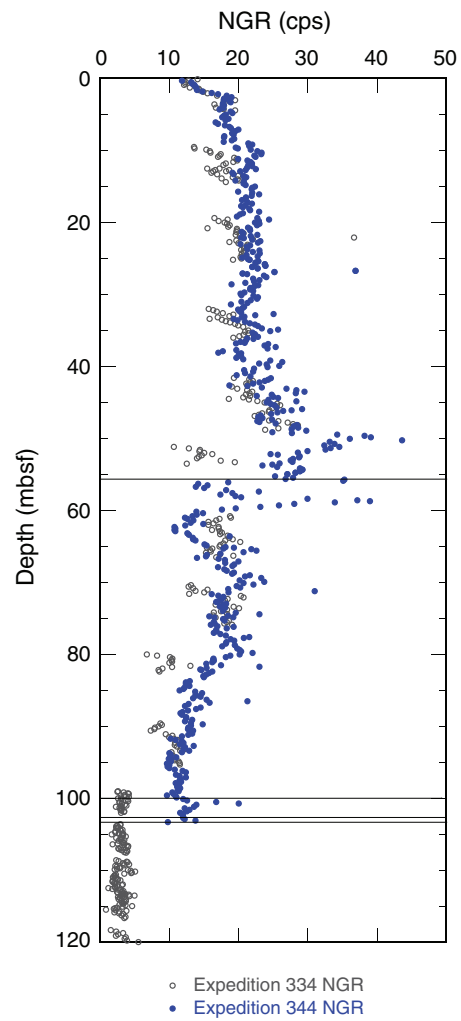


Figure F30. *P*-wave velocity, Site U1381. **A.** *P*-wave velocity measured on split cores. **B.** *P*-wave velocity measured on the Whole-Round Multisensor Logger (WRMSL). Horizontal lines = lithostratigraphic unit boundaries.

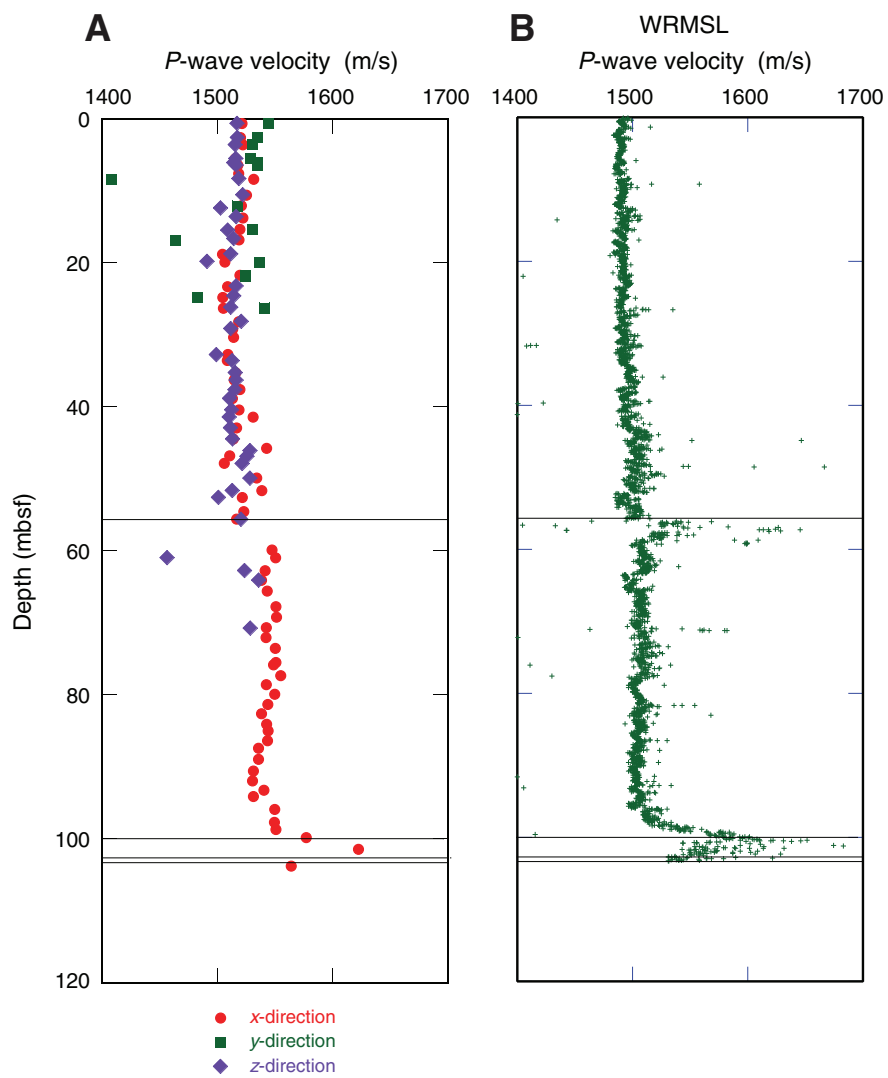


Figure F31. Thermal data, Site U1381. **A.** Thermal conductivity values. **B.** Equilibrium temperatures. Dashed line = temperature gradient, based on a least-squares fit to the combined data. Horizontal lines = lithostratigraphic unit boundaries.

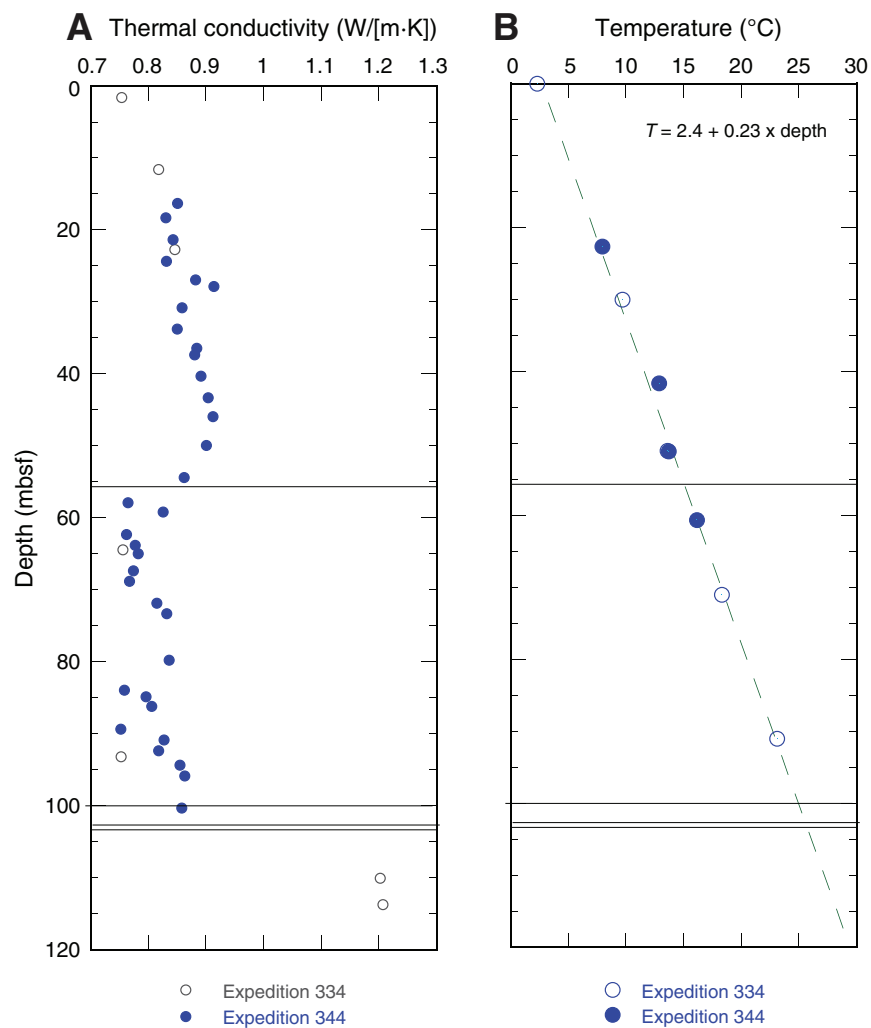


Figure F32. Strength measurements, Site U1381. Horizontal lines = lithostratigraphic unit boundaries. **A.** Un-drained shear strength measured using an automatic vane shear. **B.** Penetrometer measurements of compressive strength.

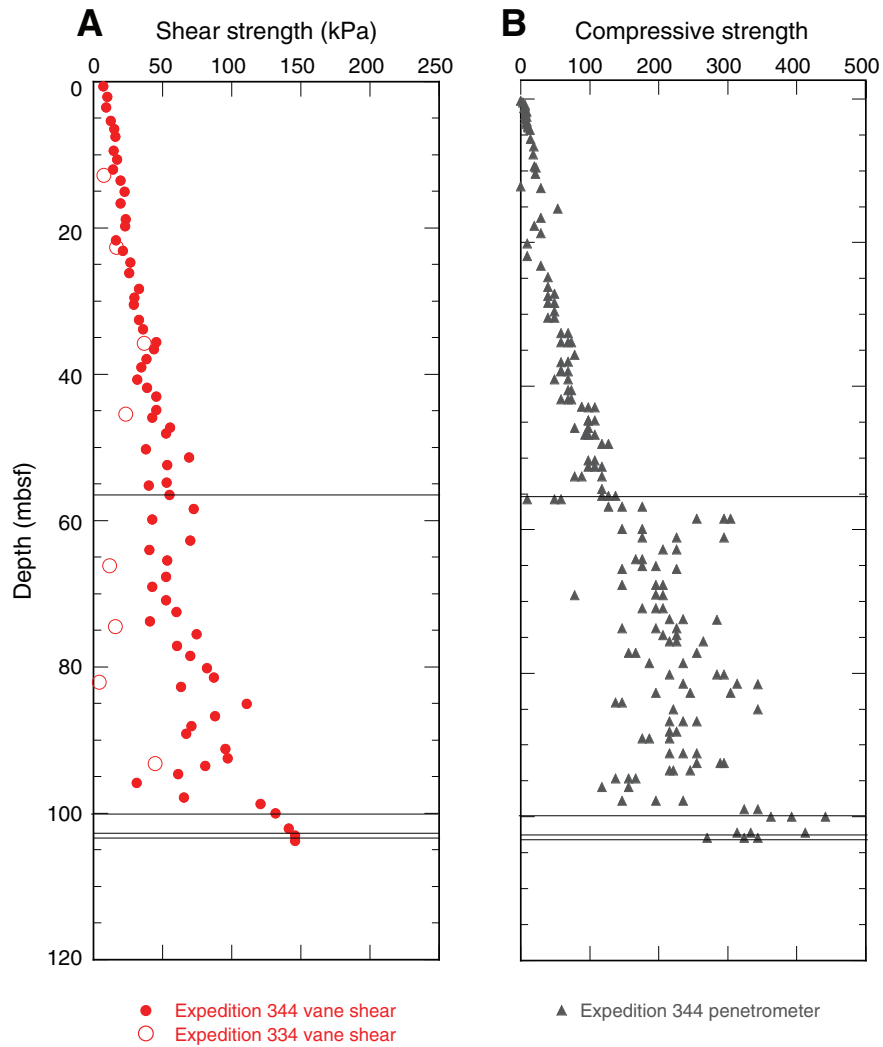


Figure F33. Electrical conductivity measurements and calculated formation factor, Site U1381. Horizontal lines = lithostratigraphic unit boundaries.

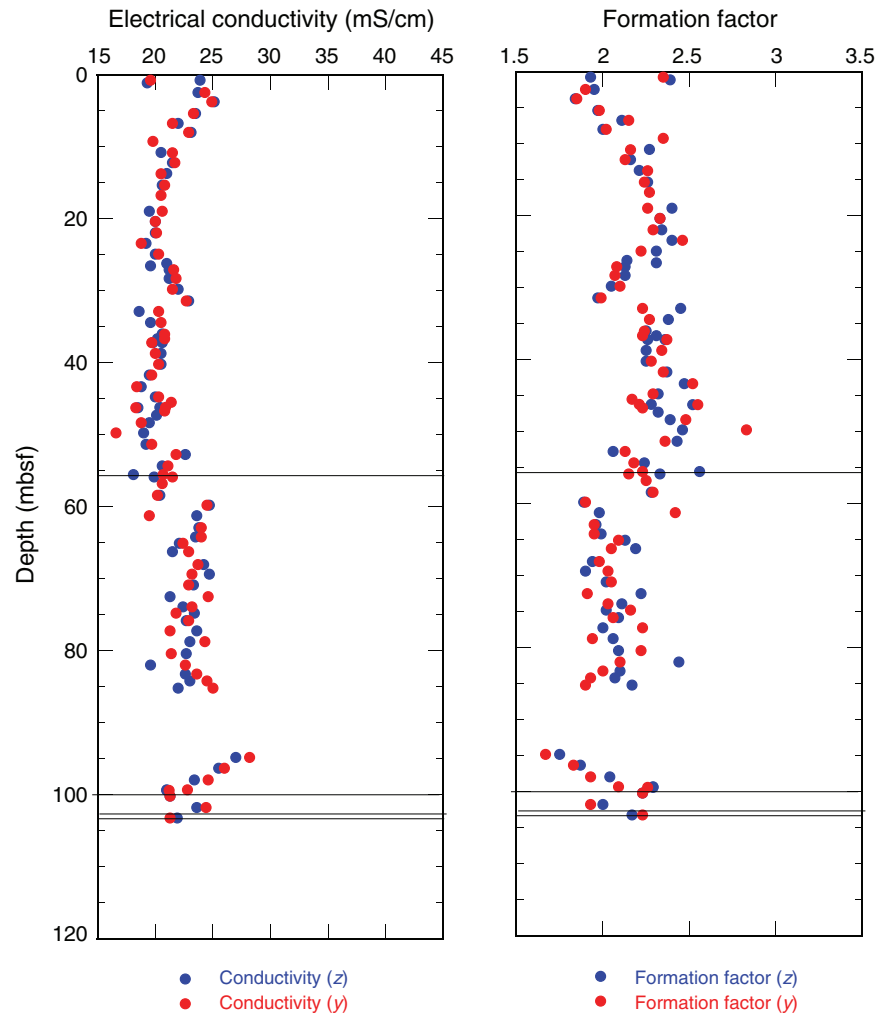


Figure F34. Reflectance L^* , a^* , and b^* profiles, Site U1381. Horizontal lines = lithostratigraphic unit boundaries.

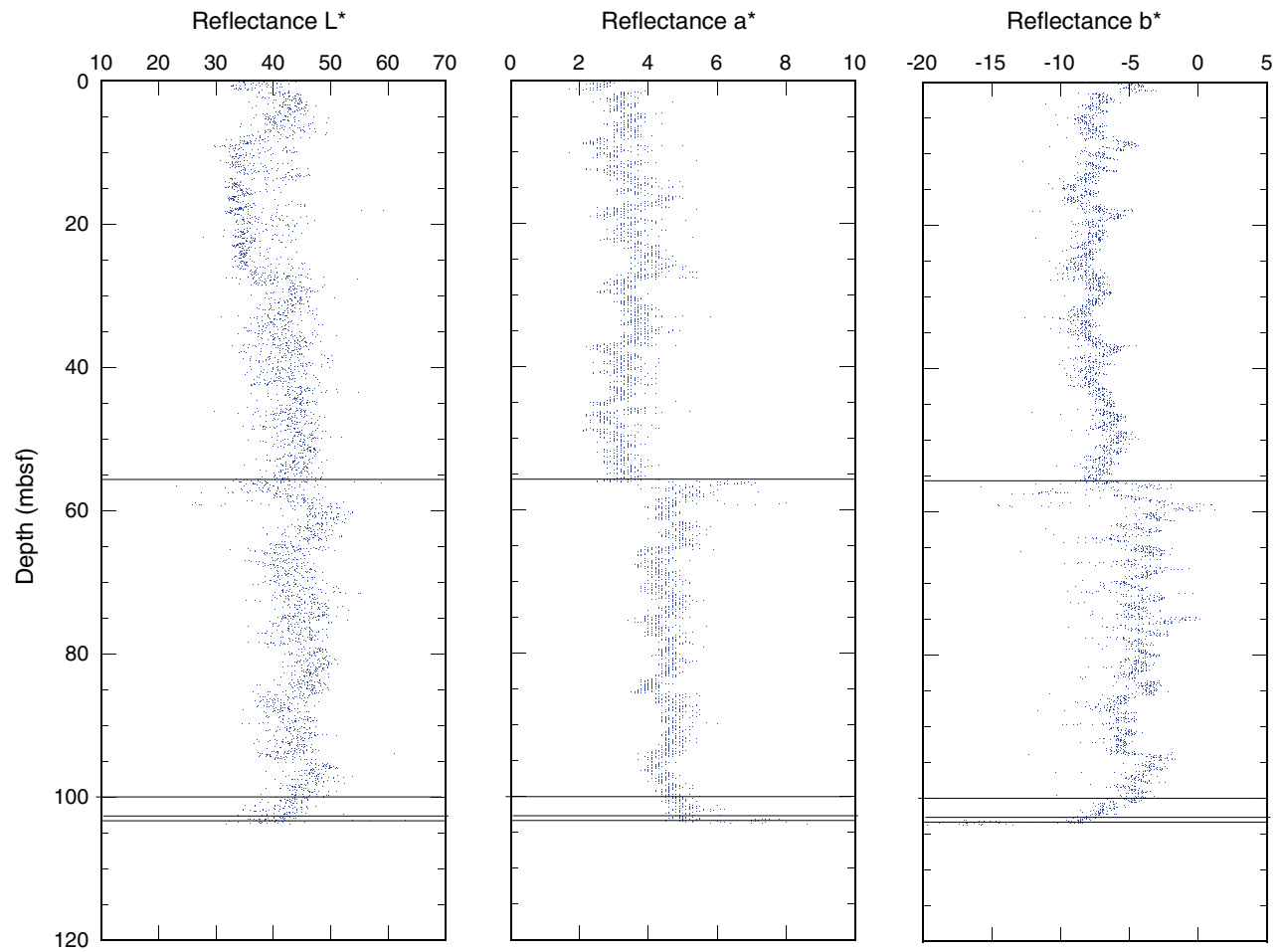


Figure F35. Paleomagnetic measurements on sediment archive-half sections, Hole U1381C. Crosses = discrete sample remanence vector end-points at the corresponding demagnetization steps. **A, B.** NRM intensity and inclination after 0 and 30 mT AF demagnetization. Yellow dashed line = expected inclination values. **C, D.** Declination before and after 30 mT AF demagnetization (black) with superimposed FlexIT orientation tool-corrected values (blue).

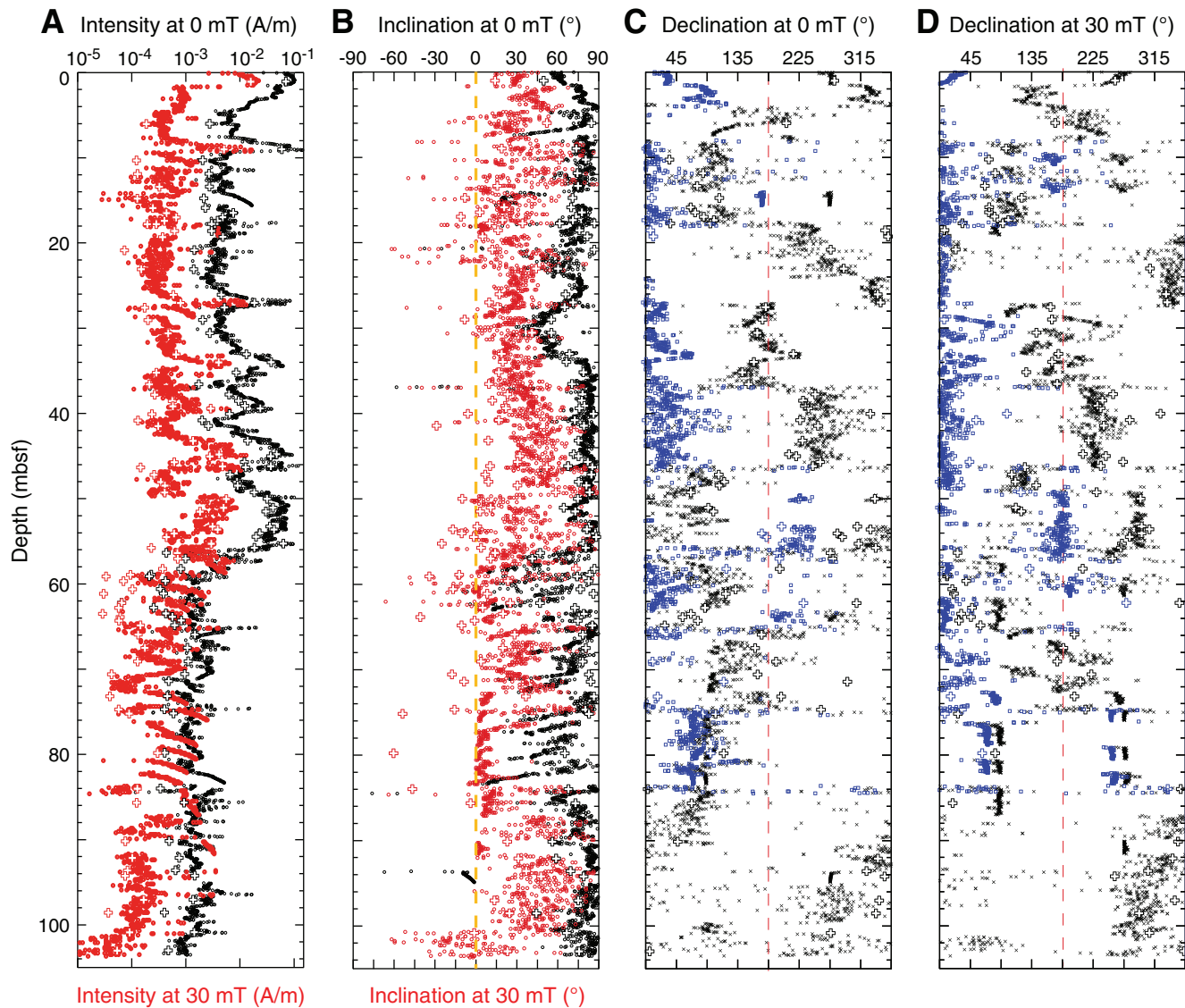


Figure F36. Representative vector end-point diagrams (Zijderveld, 1967) for sediment samples through stepwise AF demagnetization, Hole U1381C. All samples display a normal vertical component of magnetization caused by drilling that is removed after 5 mT demagnetization. Open and solid squares = projection of the magnetization vector end-points onto the vertical and horizontal planes, respectively. Blue lines = ChRM component derived by principal component analysis (PCA; Kirschvink, 1980). NRM = natural remanent magnetization. A–C. A stable component decays toward the origin of the vector plot. D–F. Less stable demagnetization behavior: negative inclinations, but declinations are still northerly.

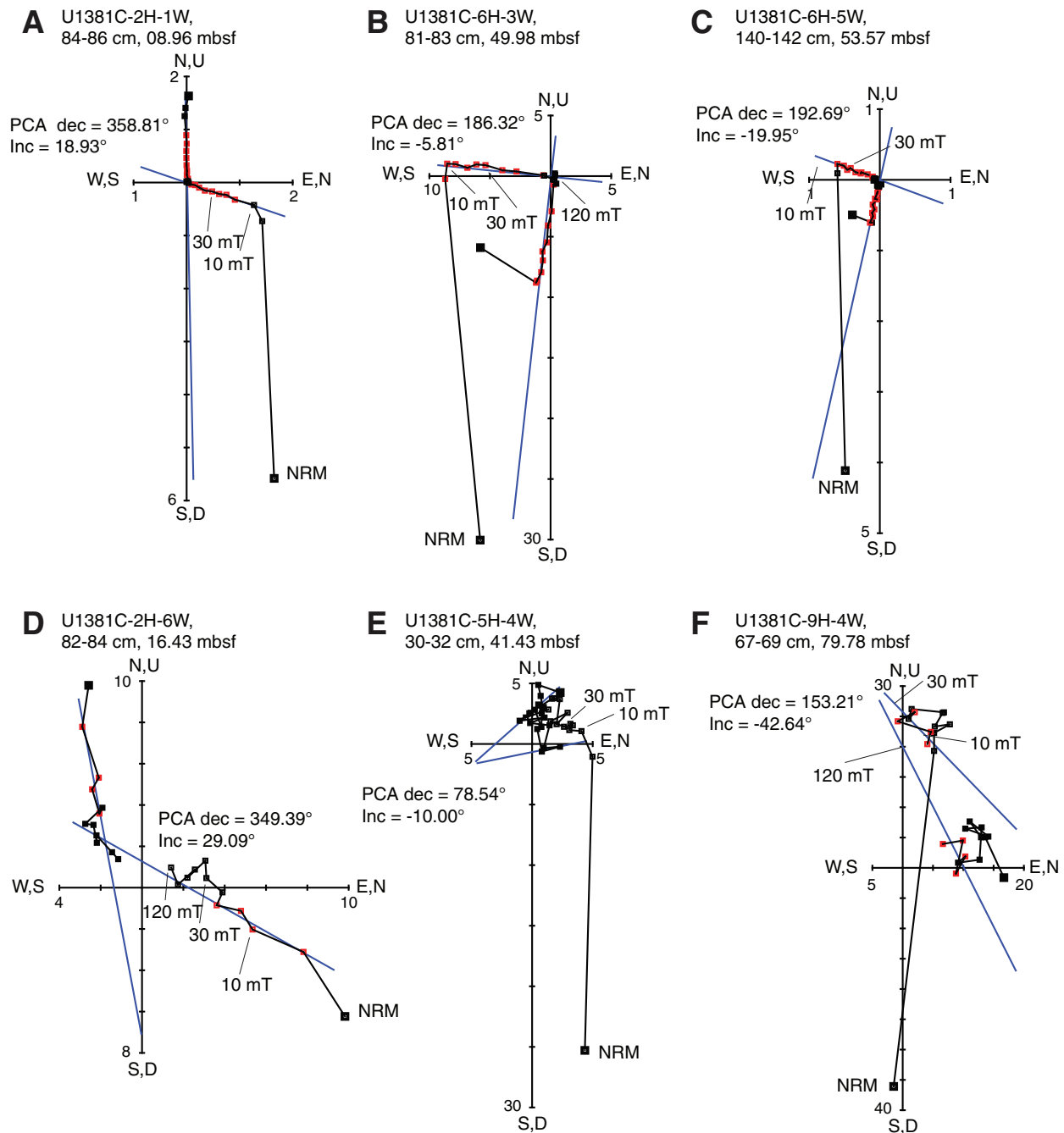


Figure F37. Discrete sample magnetostratigraphy of the uppermost 103 m after 120 mT AF demagnetization, Hole U1381C. ChRM values were determined by principal component analysis (PCA; Kirschvink, 1980). Black = normal polarity, white = reversed polarity, gray = uncertain polarity. B/M = Brunhes/Matuyama Chron. B/M = Brunhes/Matuyama Chron.

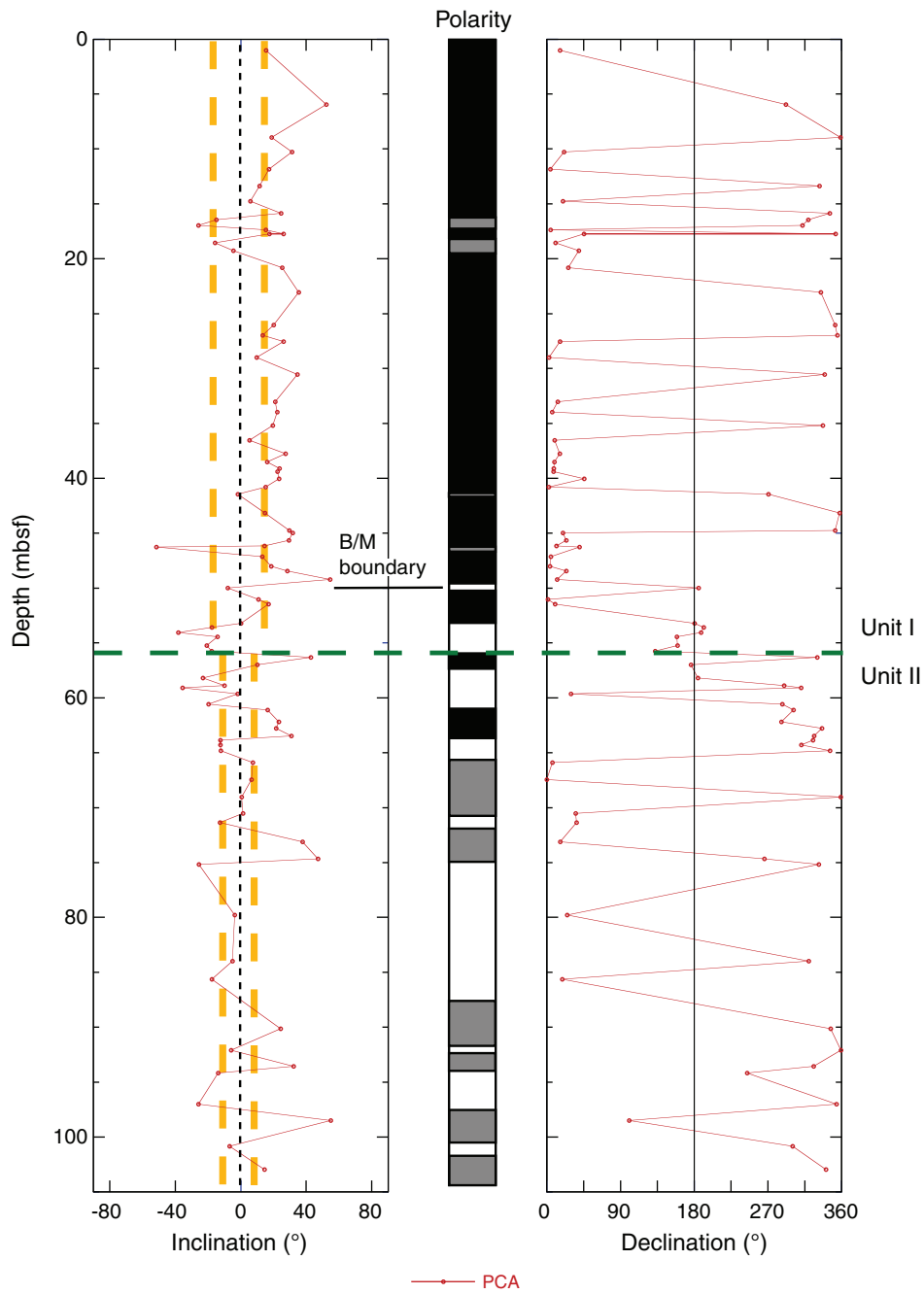


Table T1. Site U1381 coring summary.

Hole U1381C										
Latitude: 8°25.7027'N										
Longitude: 84°9.4800'W										
Time on hole (h): 33.5 (1.4 days)										
Seafloor (drill pipe measurement from rig floor, m DRF): 2075.4										
Distance between rig floor and sea level (m): 10.8										
Water depth (drill pipe measurement from sea level, m): 2064.6										
Total penetration (drilling depth below seafloor, m DSF): 103.8										
Total length of cored section (m): 103.8										
Total core recovered (m): 109.0										
Core recovery (%): 105										
Total number of cores: 13										
Core	Date (2012)	Time UTC (h)	Depth DSF (m)			Depth CSF (m)		Length of core recovered (m)	Recovery (%)	Comments
			Top of cored interval	Bottom of cored interval	Interval advanced (m)	Top of cored interval	Bottom of cored interval			
344-U1381C-										
1H	27 Oct	0225	0.00	8.10	8.1	0.00	8.16	8.16	101	FlexIT
2H	27 Oct	0333	8.10	17.60	9.5	8.10	18.11	10.01	105	FlexIT
3H	27 Oct	0425	17.60	27.10	9.5	17.60	27.66	10.06	106	FlexIT, APCT-3
4H	27 Oct	0505	27.10	36.60	9.5	27.10	37.16	10.06	106	FlexIT
5H	27 Oct	0610	36.60	46.10	9.5	36.60	46.62	10.02	105	FlexIT, APCT-3
6H	27 Oct	0715	46.10	55.60	9.5	46.10	56.13	10.03	106	FlexIT, APCT-3
7H	27 Oct	0825	55.60	65.10	9.5	55.60	65.66	10.06	106	FlexIT, APCT-3
8H	27 Oct	0920	65.10	74.60	9.5	65.10	75.13	10.03	106	FlexIT
9H	27 Oct	1040	74.60	84.10	9.5	74.60	84.50	9.90	104	FlexIT
10H	27 Oct	1130	84.10	93.60	9.5	84.10	94.01	9.91	104	
11H	27 Oct	1215	93.60	103.10	9.5	93.60	103.61	10.01	105	
12H	27 Oct	1250	103.10	103.50	0.4	103.10	103.55	0.45	113	
13X	27 Oct	1455	103.50	103.80	0.3	103.50	103.83	0.33	110	
Hole U1381C totals:					103.8			109.03	105	

DSF = drilling depth below seafloor, CSF = core depth below seafloor. H = advanced piston corer core, X = extended core barrel core. APCT-3 = advanced piston corer temperature tool.

Table T2. Summary of Hole U1381C lithologic units.

Unit	Top depth (mbsf)	Core, section, interval (cm)	Bottom depth (mbsf)	Core, section, interval (cm)	Unit thickness (m)	Major lithology
		344-U1381C-		344-U1381C-		
I	0.0	1H-1, 0	55.93	7H-1, 33	55.93	Silty clay
II	55.93	7H-1, 33	100.64	11H-5, 104	44.71	Foraminiferal nannofossil-rich calcareous ooze with spicules
III	100.64	11H-5, 104	103.20	12H-1, 10	2.56	Calcareous nannofossil-rich clay
IV	103.20	12H-1, 10	103.55	12H-CC, 16	0.35	Claystone
V	103.55	13X-1, 0	103.83	13X-1, 33	0.33	Basalt breccia



Table T3. Calcareous nannofossil faunal distribution, Hole U1381C.

Core, section, interval (cm)	Depth (mbsf)		Preservation	Group	Abundance	Taxon															
	Top	Bottom																			
344-U1381C-																					
1H-CC	8.09	8.14	M	C	Freq		Freq														
2H-CC	18.06	18.11	M	C	Freq		C														
3H-CC	27.61	27.66	G	A	C	R	A	*													
4H-CC	37.11	37.16	G	A	C		C														
5H-CC	46.57	46.62	G	D	C	R	C														
6H-7W, 15-16	55.31	55.32	M	C	C		R		*												
6H-CC	56.08	56.13	G	C	Freq	R	Freq	*													
7H-1W, 25-26	55.85	55.86	M	A	C		C														
7H-1W, 31-32	55.91	55.92	M	C	C		C		Freq												
7H-1W, 39-40	55.99	56.00	M	C			C		R												
7H-1W, 72-73	56.32	56.33	G	C	Freq		C		A												
7H-1W, 102-103	56.62	56.63	G	A	Freq		C		C												
7H-1W, 122-123	56.82	56.83	G	A	C		C		C												
7H-1W, 144-145	57.04	57.05	G	C			C		C												
7H-CC	65.61	65.66	G	C	Freq		Freq		Freq												
8H-CC	75.08	75.13	G	C	R		Freq		C												
9H-CC	84.45	84.50	G	C	Freq		C		C												
10H-CC	93.96	94.01	G	C	R		R		Freq												
11H-CC	103.56	103.61	G	C	Freq		Freq		Freq												
12H-CC	103.39	103.41	P	R			R		C												

* = reworked. Preservation: G = good, M = moderate, P = poor. Abundance: D = dominant, A = abundant, C = common, Freq = frequent, R = rare.

Table T6. Pore fluid major element concentrations, Hole U1381C.

Core, section, interval (cm)	Depth (mbsf)	Volume (mL)	Salinity	pH	Alkalinity (mM)	SO ₄ IC (mM)	SO ₄ ICP (mM)	Cl titr. (mM)	Cl IC (mM)	Br (mM)	Na (mM)	K (mM)	Ca (mM)	Mg (mM)	NH ₄ (mM)
344-U1381C-															
1H-1, 140–150	1.45	48	35.0	7.56	4.918	26.78	26.47	557	550	0.902	473	12.2	9.57	49.5	0.287
1H-3, 140–150	4.45	62	35.0	7.65	8.451	21.11	23.89	556	562	0.921	475	12.3	8.74	50.0	0.510
1H-5, 140–150	7.45	55	35.0	7.58	11.172	21.04	21.96	554	561	0.902	462	11.7	7.52	48.8	0.800
2H-4, 140–150	14.05	67	35.0	7.54	14.521	16.93	17.33	558	564	0.924	467	11.7	6.22	48.6	1.21
2H-6, 140–150	17.05	60	35.0	7.57	15.689	15.45	15.45	563	559	0.890	470	12.2	5.84	48.1	1.40
3H-2, 140–150	20.55	64	35.0	7.73	16.377	14.13	14.33	562	563	0.899	470	11.6	5.41	47.6	1.41
3H-4, 140–150	23.55	60	34.5	7.49	16.930	13.36	13.59	565	563	0.904	485	12.0	5.38	49.1	1.51
3H-6, 140–150	26.55	72	33.5	7.60	17.432	12.72	13.12	567	562	0.900	468	11.8	5.08	48.0	1.50
4H-3, 140–150	31.55	59	33.5	7.52	17.443	12.29	12.31	563	563	0.902	484	11.8	5.19	48.1	1.60
4H-5, 140–150	34.55	58	34.5	7.45	17.341	12.14	12.41	567	561	0.900	467	11.3	5.00	46.7	1.60
5H-3, 140–150	41.07	57	34.0	7.55	16.361	12.04	13.00	567	542	0.865	473	11.3	5.19	47.6	1.52
5H-6, 140–150	45.57	57	34.0	7.57	15.194	12.67	13.36	566	545	0.870	473	11.4	5.13	48.0	1.49
6H-3, 135–150	50.59	60	34.0	7.44	13.278	14.23	14.57	568	560	0.897	470	11.4	5.27	48.3	ND
6H-6, 135–150	55.09	60	33.5	7.49	11.712	15.25	15.41	566	566	0.906	467	11.4	5.44	48.0	1.26
7H-3, 135–150	60.03	75	34.0	7.40	9.973	16.93	17.11	569	567	0.903	469	11.0	5.84	49.4	1.20
7H-6, 135–150	64.53	70	34.0	7.39	9.176	17.29	17.66	563	561	0.898	474	11.0	6.17	49.3	1.18
8H-3, 136–151	69.55	70	34.0	7.42	8.089	18.41	19.58	568	564	0.894	472	10.8	6.98	49.4	0.829
8H-6, 135–150	74.07	72	34.0	7.38	7.419	19.02	19.81	565	560	0.887	472	10.7	7.68	49.5	0.848
9H-3, 135–150	79.03	72	34.0	7.35	6.482	20.15	21.16	570	561	0.888	470	10.6	8.68	49.3	0.744
9H-6, 135–150	83.53	69	34.0	7.38	6.031	21.11	21.70	566	567	0.899	466	10.5	9.57	49.2	0.653
10H-2, 140–150	87.05	67	34.0	7.34	5.416	21.93	22.53	563	563	0.890	470	10.2	10.8	48.5	0.569
10H-3, 140–150	88.55	68	34.0	7.40	5.055	22.03	22.47	563	561	0.890	475	10.4	11.1	49.1	0.481
10H-5, 140–150	91.55	69	34.0	7.37	4.827	22.24	22.81	563	555	0.875	472	10.2	11.9	48.2	0.502
10H-6, 140–150	93.05	54	34.0	7.37	4.616	22.90	22.95	566	565	0.895	484	10.7	12.3	48.9	0.506
11H-2, 140–150	96.55	56	34.3	7.44	3.924	26.93	23.68	566	556	0.860	480	10.6	13.7	48.7	0.463
11H-3, 140–150	98.05	48	34.0	7.41	3.630	23.66	24.32	563	564	0.896	469	10.2	13.8	46.8	0.411
11H-5, 140–150	101.05	24	33.5	ND	2.685	24.89	24.19	561	561	0.885	473	9.65	15.2	48.5	0.357
11H-6, 140–150	102.55	22	33.5	ND	ND	25.04	25.76	557	551	0.868	478	9.81	16.2	48.3	0.290

IC = ion chromatograph, ICP = inductively coupled plasma–atomic emission spectroscopy, titr. = titration, ND = not detected.

Table T7. Pore fluid minor element concentrations, Hole U1381C.

Core, section, interval (cm)	Depth (mbsf)	B (μM)	Li (μM)	Sr (μM)	Ba (mM)	Mn (μM)	Si (μM)	PO ₄ (μM)
344-U1381C-								
1H-1, 140-150	1.45	541	24.7	83.0	0.216	13	523	10.0
1H-3, 140-150	4.45	541	22.4	83.7	0.306	6.2	604	17.1
1H-5, 140-150	7.45	544	21.9	80.8	0.304	4.6	609	20.3
2H-4, 140-150	14.05	555	22.0	81.2	0.241	3.0	652	25.5
2H-6, 140-150	17.05	543	21.0	79.8	0.325	3.1	666	13.5
3H-2, 140-150	20.55	539	22.6	81.4	0.376	2.0	707	13.0
3H-4, 140-150	23.55	520	23.0	83.1	0.426	2.2	624	12.5
3H-6, 140-150	26.55	510	23.4	81.3	0.373	2.2	649	14.2
4H-3, 140-150	31.55	510	24.6	82.3	0.456	3.2	699	37.6
4H-5, 140-150	34.55	513	25.0	82.0	0.476	3.3	718	36.4
5H-3, 140-150	41.07	509	27.3	84.8	0.466	3.9	750	33.1
5H-6, 140-150	45.57	491	29.1	86.3	0.412	3.8	749	24.3
6H-3, 135-150	50.59	473	31.5	88.0	0.451	3.3	740	13.5
6H-6, 135-150	55.09	478	32.6	90.5	0.536	3.7	735	8.3
7H-3, 135-150	60.03	463	33.3	92.0	0.291	4.2	749	6.0
7H-6, 135-150	64.53	459	35.2	94.1	0.151	4.6	832	3.8
8H-3, 136-151	69.55	456	35.5	96.9	0.295	4.7	724	2.1
8H-6, 135-150	74.07	457	35.1	98.5	0.167	4.8	827	1.8
9H-3, 135-150	79.03	451	37.3	103	0.320	4.7	883	1.8
9H-6, 135-150	83.53	453	37.7	105	0.138	5.0	907	1.7
10H-2, 140-150	87.05	444	37.7	106	0.222	5.7	957	1.6
10H-3, 140-150	88.55	447	38.8	107	0.346	5.9	874	1.6
10H-5, 140-150	91.55	442	38.3	105	0.296	6.6	848	1.4
10H-6, 140-150	93.05	446	39.5	108	0.253	6.6	977	1.9
11H-2, 140-150	96.55	435	38.3	107	0.511	7.6	972	3.3
11H-3, 140-150	98.05	426	38.6	106	0.251	7.1	1026	1.0
11H-5, 140-150	101.05	376	36.9	105	0.342	7.2	957	ND
11H-6, 140-150	102.55	363	37.8	104	0.381	7.8	919	1.4

ND = not detected.

Table T8. Concentrations of hydrocarbon gases in headspace gas samples, Hole U1381C.

Core, section, interval (cm)	Depth (mbsf)	Methane (ppmv)	Ethane (ppmv)	Propane (ppmv)
344-U1381C-				
1H-2, 0-5	1.50	262	256	223
1H-4, 0-5	4.50	4.36	1.77	ND
1H-6, 0-5	7.50	6.30	2.25	ND
2H-3, 0-5	11.10	3.09	ND	ND
2H-5, 0-5	14.10	5.33	ND	ND
2H-7, 0-5	17.10	4.48	ND	ND
3H-3, 0-5	20.60	5.16	ND	ND
3H-5, 0-5	23.60	3.69	ND	ND
3H-7, 0-5	26.60	3.80	ND	ND
4H-4, 0-5	31.60	5.14	ND	ND
4H-6, 0-5	34.60	5.88	ND	ND
5H-4, 0-5	41.12	6.80	ND	ND
5H-7, 0-5	45.62	5.91	ND	ND
6H-4, 0-5	50.66	5.73	ND	ND
6H-7, 0-5	55.16	4.91	ND	ND
7H-4, 0-5	60.10	4.39	ND	ND
7H-7, 0-5	64.60	4.40	ND	ND
8H-4, 0-5	69.62	4.05	ND	ND
8H-7, 0-5	74.14	4.11	ND	ND
9H-4, 0-5	79.10	4.21	ND	ND
9H-7, 0-5	83.60	3.58	ND	ND
10H-3, 0-5	87.10	3.10	ND	ND
10H-4, 0-5	88.60	3.09	ND	ND
10H-6, 0-5	91.60	3.14	ND	ND
10H-7, 0-5	93.10	3.58	ND	ND
11H-2, 0-5	96.60	3.44	ND	ND
11H-4, 0-5	98.10	3.53	ND	ND
11H-6, 0-5	101.10	ND	ND	ND
11H-7, 0-5	102.60	2.13	ND	ND

ND = not detected.

Table T9. Inorganic carbon (IC), total carbon (TC), total organic carbon (TOC), calcium carbonate, and total nitrogen (TN), Hole U1381C.

Core, section, interval (cm)	Depth (mbsf)	IC (wt%)	TC (wt%)	TOC (wt%)	CaCO ₃ (wt%)	TN (wt%)
344-U1381C-						
1H-1, 38–39	0.387	1.36	3.44	2.08	11.4	0.197
1H-3, 46–47	3.445	0.196	2.02	1.82	1.63	0.167
1H-3, 140–141	4.378	0.414	2.39	1.98	3.46	0.184
1H-5, 136–137	7.316	0.205	2.02	1.82	1.71	0.156
2H-3, 0–1	10.956	0.868	2.75	1.88	7.24	0.157
2H-4, 68–70	13.035	0.739	2.30	1.56	6.17	0.135
2H-4, 139–140	13.700	0.499	2.48	1.98	4.16	0.157
2H-6, 47–49	15.683	0.172	1.62	1.45	1.44	0.131
4H-2, 124–125	29.696	1.17	2.58	1.41	9.75	0.126
4H-3, 61–62	30.518	0.609	1.92	1.31	5.08	0.117
4H-3, 136–137	31.227	0.625	2.13	1.51	5.22	0.135
5H-3, 39–40	39.842	1.03	2.22	1.19	8.58	0.115
5H-5, 135–135	43.588	0.583	1.47	0.887	4.86	0.080
5H-6, 24–25	43.967	1.50	2.50	0.998	12.5	0.096
6H-3, 33–34	49.320	2.21	3.24	1.03	18.5	0.077
6H-4, 131–132	51.669	3.92	5.19	1.27	32.7	0.078
6H-6, 62–63	53.858	2.83	3.80	0.967	23.6	0.075
6H-6, 134–135	54.540	2.58	3.60	1.02	21.5	0.073
7H-3, 134–135	59.708	5.27	6.63	1.36	44.0	0.068
7H-4, 5–6	59.906	4.74	6.11	1.37	39.5	0.065
7H-6, 124–125	63.862	5.00	6.39	1.39	41.7	0.061
8H-3, 28–29	68.226	4.84	6.62	1.78	40.4	0.091
8H-3, 134–135	69.230	4.10	5.99	1.89	34.2	0.086
8H-6, 133–134	73.511	5.66	7.30	1.64	47.2	0.080
9H-3, 120–121	78.640	4.78	6.62	1.84	39.9	0.102
9H-6, 122–123	82.977	4.82	6.63	1.81	40.2	0.091
10H-2, 139–140	86.880	3.31	5.17	1.86	27.6	0.103
10H-3, 118–119	88.117	4.27	6.20	1.93	35.6	0.102
10H-5, 139–140	91.194	5.62	7.68	2.06	46.9	0.105
10H-6, 139–140	92.631	4.82	6.90	2.08	40.2	0.111
11H-2, 138–139	96.343	5.18	6.50	1.32	43.2	0.049
11H-3, 138–139	97.766	5.50	6.96	1.46	45.8	0.061
11H-4, 133–134	99.143	5.14	6.57	1.43	42.9	0.059
11H-4, 133–134	99.143	4.85	6.23	1.38	40.4	0.059
11H-5, 140–141	100.633	5.21	7.17	1.96	43.4	0.087
11H-6, 140–141	102.056	4.33	6.33	2.00	36.1	0.092